arXiv:2203.02694v1 [astro-ph.EP] 5 Mar 2022

TOI-1696: a nearby M4 dwarf with a $3R_\oplus$ planet in the Neptunian desert

Mayuko Mori [ID],[1] John H. Livingston [ID],[1,2,3] Jerome de Leon [ID],[1] Norio Narita [ID],[4,2,5]
Teruyuki Hirano [ID],[2,3,6] Akihiko Fukui [ID],[4,5] Karen A. Collins [ID],[7] Naho Fujita [ID],[8]
Yasunori Hori [ID],[2,3] Hiroyuki Tako Ishikawa [ID],[2,3] Kiyoe Kawauchi [ID],[5,9]
Keivan G. Stassun [ID],[10] Noriharu Watanabe [ID],[11] Steven Giacalone [ID],[12] Rebecca Gore,[12]
Ashley Schroeder,[12] Courtney D. Dressing [ID],[13] Allyson Bieryla [ID],[7] Eric L. N. Jensen [ID],[14]
Bob Massey [ID],[15] Avi Shporer [ID],[16] Masayuki Kuzuhara [ID],[2,3] David Charbonneau [ID],[7]
David R. Ciardi [ID],[17] John P. Doty,[18] Emma Esparza-Borges [ID],[5,9] Hiroki Harakawa,[19]
Klaus Hodapp [ID],[20] Masahiro Ikoma [ID],[3,6] Kai Ikuta [ID],[11] Keisuke Isogai [ID],[21,11]
Jon M. Jenkins [ID],[22] Taiki Kagetani [ID],[11] Tadahiro Kimura,[23] Takanori Kodama [ID],[4]
Takayuki Kotani,[2,3,6] Vigneshwaran Krishnamurthy [ID],[2,3] Tomoyuki Kudo [ID],[19]
Seiya Kurita,[23] Takashi Kurokawa,[2,24] Nobuhiko Kusakabe [ID],[2,3] David W. Latham [ID],[7]
Brian McLean,[25] Felipe Murgas [ID],[5,9] Jun Nishikawa [ID],[3,6,2] Taku Nishiumi [ID],[6,2,11]
Masashi Omiya,[2,3] Hugh P. Osborn [ID],[16,26] Enric Palle [ID],[5,9] Hannu Parviainen [ID],[5,9]
George R. Ricker [ID],[16] Sara Seager [ID],[27,16,28] Takuma Serizawa,[24,3] Motohide Tamura [ID],[1,2,3]
Huan-Yu Teng [ID],[29] Yuka Terada [ID],[30,31] Joseph D. Twicken [ID],[22,32] Akitoshi Ueda,[2,3,6]
Roland Vanderspek [ID],[16] Sébastien Vievard [ID],[19,2] Joshua N. Winn [ID],[33] and Yujie Zou [ID][11]

[1]*Department of Astronomy, Graduate School of Science, The University of Tokyo, 7-3-1 Hongo, Bunkyo, Tokyo 113-0033, Japan*

[2]*Astrobiology Center, 2-21-1 Osawa, Mitaka, Tokyo 181-8588, Japan*

[3]*National Astronomical Observatory of Japan, 2-21-1 Osawa, Mitaka, Tokyo 181-8588, Japan*

[4]*Komaba Institute for Science, The University of Tokyo, 3-8-1 Komaba, Meguro, Tokyo 153-8902, Japan*

[5]*Instituto de Astrofísica de Canarias (IAC), 38205 La Laguna, Tenerife, Spain*

[6]*Department of Astronomy, School of Science, The Graduate University for Advanced Studies (SOKENDAI), 2-21-1 Osawa, Mitaka, Tokyo, Japan*

[7]*Center for Astrophysics | Harvard & Smithsonian, 60 Garden Street, Cambridge, MA 02138, USA*

[8]*Department of Astronomy, Kyoto University, Kitashirakawa-Oiwake-cho, Sakyo-ku, Kyoto 606-8502, Japan*

[9]*Departamento de Astrofísica, Universidad de La Laguna (ULL), 38206 La Laguna, Tenerife, Spain*

[10]*Department of Physics and Astronomy, Vanderbilt University, Nashville, TN 37235, USA*

[11]*Department of Multi-Disciplinary Sciences, Graduate School of Arts and Sciences, The University of Tokyo, 3-8-1 Komaba, Meguro, Tokyo 153-8902, Japan*

[12]*Department of Astronomy, University of California Berkeley, Berkeley, CA 94720, USA*

[13]*Department of Astronomy, The University of California, Berkeley, CA 94720, USA*

[14]*Department of Physics & Astronomy, Swarthmore College, Swarthmore PA 19081, USA*

[15]*Villa '39 Observatory, Landers, CA 92285, USA*

[16]*Department of Physics and Kavli Institute for Astrophysics and Space Research, Massachusetts Institute of Technology, Cambridge, MA 02139, USA*

[17]*Caltech/IPAC-NASA Exoplanet Science Institute, 770 S. Wilson Avenue, Pasadena, CA 91106, USA*

[18]*Noqsi Aerospace Ltd., 15 Blanchard Avenue, Billerica, MA 01821, USA*

[19]*Subaru Telescope, 650 N. Aohoku Place, Hilo, HI 96720, USA*

[20]*University of Hawaii, Institute for Astronomy, 640 N. Aohoku Place, Hilo, HI 96720, USA*

[21]*Okayama Observatory, Kyoto University, 3037-5 Honjo, Kamogatacho, Asakuchi, Okayama 719-0232, Japan*

[22]*NASA Ames Research Center, Moffett Field, CA 94035, USA*

[23]*Department of Earth and Planetary Science, Graduate School of Science, The University of Tokyo, 7-3-1 Hongo, Bunkyo, Tokyo 113-0033, Japan*

Corresponding author: Mayuko Mori

mori@astron.s.u-tokyo.ac.jp

[24] *Institute of Engineering, Tokyo University of Agriculture and Technology, 2-24-16, Naka-cho, Koganei, Tokyo, 184-8588, Japan*

[25] *Space Telescope Science Institute, 3700 San Martin Drive, Baltimore, MD, 21218, USA*

[26] *NCCR/Planet-S, Universität Bern, Gesellschaftsstrasse 6, 3012 Bern, Switzerland*

[27] *Department of Earth, Atmospheric, and Planetary Sciences, Massachusetts Institute of Technology, Cambridge, MA 02139, USA*

[28] *Department of Aeronautics and Astronautics, Massachusetts Institute of Technology, Cambridge, MA 02139, USA*

[29] *Department of Earth and Planetary Sciences, School of Science, Tokyo Institute of Technology, 2-12-1 Ookayama, Meguro-ku, Tokyo 152-8551, Japan*

[30] *Institute of Astronomy and Astrophysics, Academia Sinica, P.O. Box 23-141, Taipei 10617, Taiwan, R.O.C.*

[31] *Department of Astrophysics, National Taiwan University, Taipei 10617, Taiwan, R.O.C.*

[32] *SETI Institute, Mountain View, CA 94043, USA*

[33] *Department of Astrophysical Sciences, Princeton University, 4 Ivy Lane, Princeton, NJ 08544, USA*

ABSTRACT

We present the discovery and validation of a temperate sub-Neptune around the nearby mid-M dwarf TIC 470381900 (TOI-1696), with a radius of 3.09 ± 0.11 $R_\oplus$ and an orbital period of 2.5 days, using a combination of *TESS* and follow-up observations using ground-based telescopes. Joint analysis of multi-band photometry from *TESS*, MuSCAT, MuSCAT3, Sinistro, and KeplerCam confirmed the transit signal to be achromatic as well as refined the orbital ephemeris. High-resolution imaging with Gemini/'Alopeke and high-resolution spectroscopy with the Subaru/IRD confirmed that there are no stellar companions or background sources to the star. The spectroscopic observations with IRD and IRTF/SpeX were used to determine the stellar parameters, and found the host star is an M4 dwarf with an effective temperature of $T_{\rm eff} = 3185 \pm 76$ K and a metallicity of [Fe/H] $= 0.336 \pm 0.060$ dex. The radial velocities measured from IRD set a 2-σ upper limit on the planetary mass to be 48.8 $M_\oplus$. The large radius ratio ($R_{\rm p}/R_\star \sim 0.1$) and the relatively bright NIR magnitude (J=12.2 mag) make this planet an attractive target for further followup observations. TOI-1696 b is one of the planets belonging to the Neptunian desert with the highest transmission spectroscopy metric discovered to date, making it an interesting candidate for atmospheric characterizations with *JWST*.

1. INTRODUCTION

Exoplanet population statistics from the *Kepler* mission (Borucki et al. 2010) revealed that there is a dearth of planets around the size of Neptune ($\sim$3–4$R_\oplus$) with orbital periods less than 2–4 d. This has been referred to as the "Neptunian Desert" or "photo-evaporation desert" or simply "evaporation desert" (Szabó & Kiss 2011; Mazeh et al. 2016; Lopez 2017). The scarcity of planets in this region of parameter space can be explained by photo-evaporation, that is, atmospheric mass loss due to high-energy irradiation from the host star (Owen & Wu 2017). The small number of planets that have so far been found in the desert (e.g. West et al. 2019; Jenkins et al. 2020) are believed to retain substantial atmospheres (or are still in the process of losing them), but the physical mechanisms are not well understood. Comparing planets that have lost their atmospheres with those that have retained their atmospheres will be useful to understand the processes such as photo-evaporation theory. Therefore, it is important to increase the number of planets in this region and reveal the nature of their atmospheres. *TESS* (Ricker et al. 2015), which has identified over 5000 exoplanet

POSSII-F (1988)
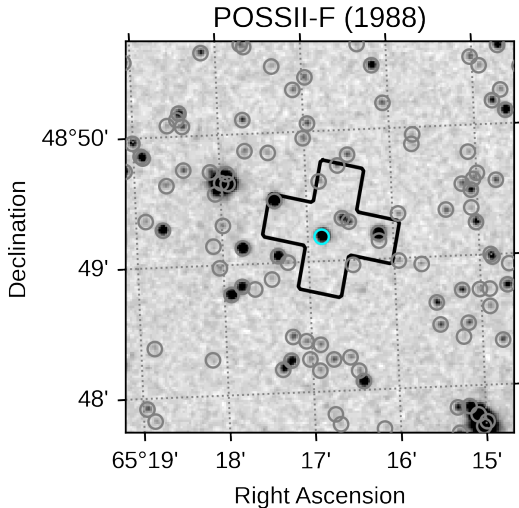
Figure 1. Archival imaging from POSSII-F survey (taken in 1998; Reid et al. 1991) with the *TESS* photometric aperture (black outline) and *Gaia* sources (gray circles). The cyan circle indicates the position of TOI-1696; we note the proper motion is low enough that its current position is not significantly offset in the archival image.

candidates so far[1], made it possible to discover more planets in the Neptunian Desert.

In this paper, we report the validation of a new planet around the mid-M dwarf TOI-1696, whose transits were identified by the *TESS* mission. The planet TOI-1696 b has a sub-Neptune size ($3.09 \pm 0.11\ R_\oplus$) and an orbital period of 2.5 days, which places it within (or near the boundaries of) the Neptunian desert.

The large radius ratio ($R_{\rm p}/R_\star \sim 0.1$) makes the planet's transits deep, and combined with the relatively bright near-IR (NIR) magnitude (J=12.2 mag) of the star, the planet is one of the best targets for future atmospheric research via transmission spectroscopy.

The rest of this paper is organized as follows. In Section 2, we present the observational data and the reduction procedures used for the analyses. In Section 3, we explain the analyses methods and results. In Section 4, we discuss the features of the planet and its future observational prospects, concluding with a summary in Section 5.

2. OBSERVATIONS & DATA REDUCTION

2.1. *Transit photometry - TESS*

TESS observed TOI-1696 with a 2 min cadence in Sector 19 from 2019 Jul 25 to Aug 22, resulting in photometry spanning approximately 27 days with a gap of about one day in the middle when the satellite reoriented itself for data downlink near perigee. Light curves were produced by the Science Processing Operations Center (SPOC) photometry pipeline (Jenkins 2002; Jenkins et al. 2010; Jenkins & et al. 2020) using the aperture shown in Figure 1. We used the PDCSAP light curves produced by the SPOC pipeline (Stumpe et al. 2012; Smith et al. 2012; Stumpe et al. 2014) for our transit analyses. TOI-1696 is located in a fairly crowded field, owing to its low galactic latitude ($b = -0.81°$). The SPOC pipeline applies a photometric dilution correction based on the CROWDSAP metric, which we independently confirmed by computing dilution values based on Gaia DR2 magnitudes[2].

TOI-1696.01 was detected by the SPOC pipeline in a transiting planet search, and the candidate was subsequently reported to the community by the *TESS* Science Office (TSO) on 2020 January 30 via the *TESS* Object of Interest (TOI; Guerrero et al. (2021)) Releases portal[3]. The candidate passed all data validation diagnostic tests (Twicken et al. 2018) performed by the SPOC[4]. The SPOC pipeline removed the transit signals of TOI-1696.01 from the light curve and performed a search for additional planet candidates (Li et al. 2019), but none were reported.

We independently confirmed the transit signal found by the SPOC. After removing stellar variability and residual instrumental systematics from the PDCSAP light curve using a 2nd order polynomial Savitzy-Golay filter, we searched for periodic transit-like signals using the transit least-squares algorithm (TLS; Hippke & Heller 2019)[5], resulting in the detection of TOI-1696.01 with a signal detection efficiency (SDE) of 11.6, a transit signal-to-noise

---

[1] As of 2022 February per https://exoplanetarchive.ipac.caltech.edu/

[2] approximating *Gaia* $R_{\rm p}$ as the *TESS* bandpass, and assuming a full width at half maximum (FWHM) of $25''$

[3] https://tess.mit.edu/toi-releases/

[4] Full vetting report available for download at https://exo.mast.stsci.edu/exomast_planet.html?planet=TOI169601

[5] https://transitleastsquares.readthedocs.io/en/latest/index.html
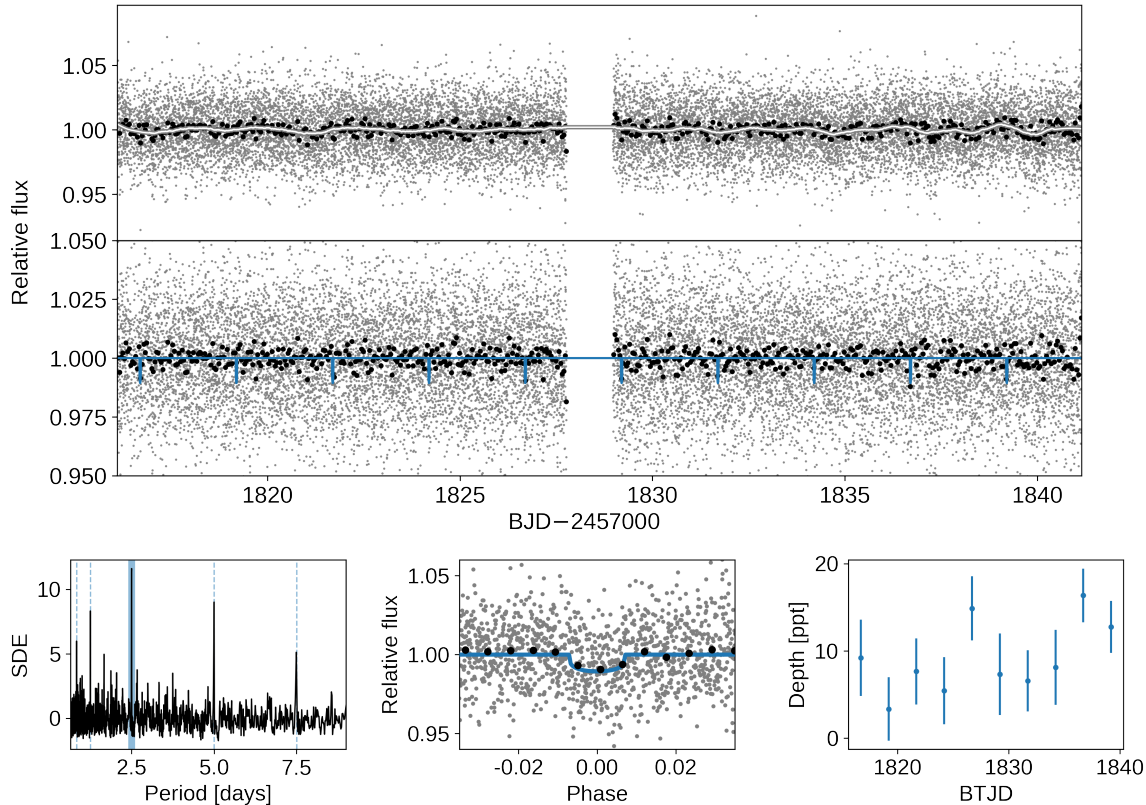
Figure 2. The upper panels show the *TESS* PDCSAP lightcurve with Savitzky-Golay (window=1001) variability model (top), and the flattened lightcurve with TLS model (bottom). The lower panels show the TLS power spectrum (left), folded *TESS* lighturve with TLS model (middle), and individual transit depths from TLS (right).

ratio (SNR) of 7.4, orbital period of 2.50031 ± 0.00001 days, and transit depth of 10.6 parts per thousand (ppt), which is consistent with the values reported by the *TESS* team on ExoFOP-TESS[6]. We subtracted this signal and repeated the transit search, but no additional signals with SDE above 10 were found. TLS also reports the approximate depths of each individual transit; we note that these transit depths and uncertainties are useful for diagnostic purposes only, as they are simplistically determined from the mean and standard deviation of the in-transit flux. The depths of the odd transits are within 1.5σ of the even transits, suggesting a low probability of either signal being caused by an eclipsing binary at twice the detected period. The TLS detection is shown in Figure 2.

2.2. *Transit photometry - FLWO/KeplerCam*

We used KeplerCam, mounted on the 1.2m telescope located at the Fred Lawrence Whipple Observatory (FLWO) atop Mt. Hopkins, Arizona, to observe a full transit on 2020 February 17. KeplerCam has a $23'.1 \times 23'.1$ field-of-view and operates in binned by 2 mode producing a pixel scale of $0.672''$. Images were obtained in the *i*-band with an exposure time of 300 seconds. A total of 29 images were collected over 144 minutes. The data were reduced using standard IDL routines and photometry was performed using the `AstroImageJ` software package (Collins et al. 2017).

2.3. *Transit photometry - LCO/SINISTRO*

We observed a full transit on 2020 November 13, using Sinistro, an optical camera mounted on a 1m telescope located at McDonald Observatory in Texas, operated by Las Cumbres Observatory (Brown et al. 2013). Sinistro has a $26'.5 \times 26'.5$ field of view with a pixel scale of $0.389''$. We observed 62 images in total during 339 minutes, using a *V*-band filter, with an exposure time of 5 min. The data were reduced

by the standard LCOGT `BANZAI` pipeline (Mc-Cully et al. 2018), and photometry was performed using `AstroImageJ` software.

2.4. Transit photometry - LCO/MuSCAT3

MuSCAT3 is a multi-band simultaneous camera installed on the 2m Faulkes Telescope North at Las Cumbres Observatory (LCO) on Haleakala, Maui (Narita et al. 2020). It has four channels, enabling simultaneous photometry in the g (400–550 nm), r (550–700 nm), i (700–820 nm) and z_s (820–920 nm) bands. Each channel has a 2048×2048 pixel CCD camera with a pixel scale of $0.27''$, providing a $9'.1 \times 9'.1$ field of view. We observed a full transit of TOI-1696.01 on 2020 December 23, from BJD 2459206.703523 to 2459206.827246. We took 36, 41, 89, and 131 exposures with exposure times of 300, 265, 120, and 80 s in the g, r, i, and z_s bands, respectively.

The data reduction was conducted by the standard LCOGT `BANZAI` pipeline. Then the differential photometry was conducted by a customized aperture-photometry pipeline for MuSCAT series (Fukui et al. 2011). The optimized aperture radii are 8, 6, 10, and 8 pixels ($2.16''$, $1.62''$, $2.7''$, and $2.16''$) for the g, r, i, and z_s bands, respectively. We optimized a set of comparison stars for each band to minimize the dispersion of the light curves. For computational efficiency, and to achieve a more uniform signal-to-noise ratio (SNR), we subsequently binned the g, r, i, and z_s data to 300, 240, 180, and 120 s, respectively.

2.5. Transit photometry - NAOJ 188cm/MuSCAT

We also observed a full transit with MuSCAT (Narita et al. 2015), which is installed on the 188cm telescope of National Astronomical Observatory of Japan (NAOJ) in Okayama, Japan. MuSCAT has a similar optical design as MuSCAT3 but has three CCD cameras for the g, r and z_s bands. On the night of 2021 July 28 we observed TOI-1696 from BJD 2459424.228358 to 2459424.30679. At that point, the r-band camera was not available due to an instrumental issue, so we observed with only the g and z_s bands, using an exposure time of 60 s for both bands.

The data reduction and differential photometry was performed using the pipeline described in Fukui et al. (2011). The optimized aperture

radii were 4 and 6 pixels ($1.44''$ and $2.16''$) for the g and z_s bands, respectively. Similarly to the MuSCAT3 data, we binned the g and z_s data to 300 and 120 s, respectively.

2.6. Speckle imaging - Gemini/'Alopeke

On the nights of 2020 December 03 and 2021 October 14, TOI-1696 was observed with the 'Alopeke speckle imager (Scott 2019), mounted on the 8.1 m Gemini North telescope on Mauna Kea. 'Alopeke simultaneously acquires data in two bands centered at 562 nm and 832 nm using high speed electron-multiplying CCDs (EMCCDs). We collected and reduced the data following the procedures described in Howell et al. (2011). The resulting reconstructed image achieved a contrast of Δmag = 5.8 at a separation of $1''$ in the 832 nm band. No secondary sources were detected. The data taken on 2021 October 14 is shown in Figure 3.

2.7. Adaptive optics imaging - Palomar/PHARO

On 2021 September 19 we conducted near-infrared high-resolution imaging using the adaptive optics instrument PHARO mounted on the 5 m Hale telescope at Palomar Observatory (Hayward et al. 2001). We observed TOI-1696 seperately in the $Br\gamma$ ($2.18\,\mu$m) and H_{cont} ($2.29\,\mu$m) bands, reaching a contrast of Δmag = 8 at a separation of $1''$ in both bands. The AO images and corresponding contrast curves are shown in Figure 4.

2.8. High-resolution spectroscopy - Subaru/IRD

We obtained high-resolution spectra of TOI-1696 in the NIR with IRD (Tamura et al. 2012; Kotani et al. 2018), mounted on the 8.2 m Subaru telescope. IRD can achieve a spectral resolution of ~70,000 in the wavelength range 930 nm to 1740 nm. The derived spectra were used for the three purposes: to search for spectral companions (e.g. SB2 scenarios), to measure fundamental stellar parameters (e.g. effective temperature and metallicity), and to rule out large radial velocity (RV) variations that would indicate an eclipsing binary (EB), as well as placing a limit on the mass of the planet. From UT 2021 January 30 to 2022 January 08, we obtained 13 spectra of TOI-1696 using 1800 s exposure times, as part of a Subaru Intensive Program (Proposal IDs S20B-
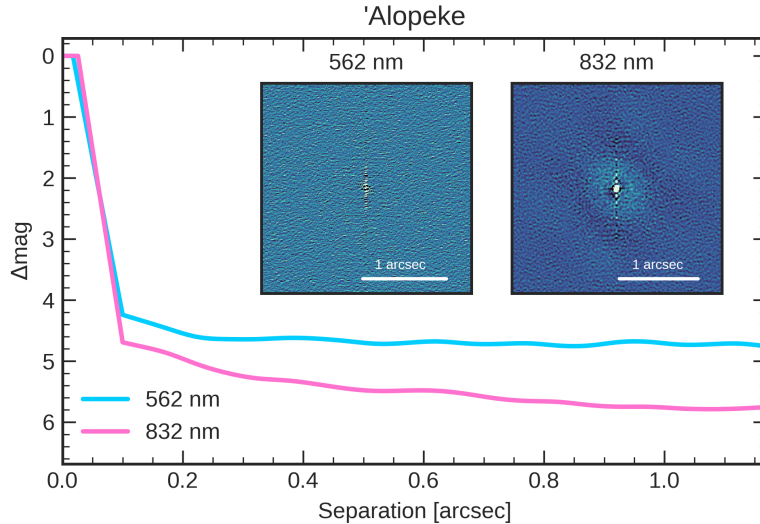
Figure 3. Gemini/'Alopeke reconstructed images and contrast curves produced as described in Section 2.6.
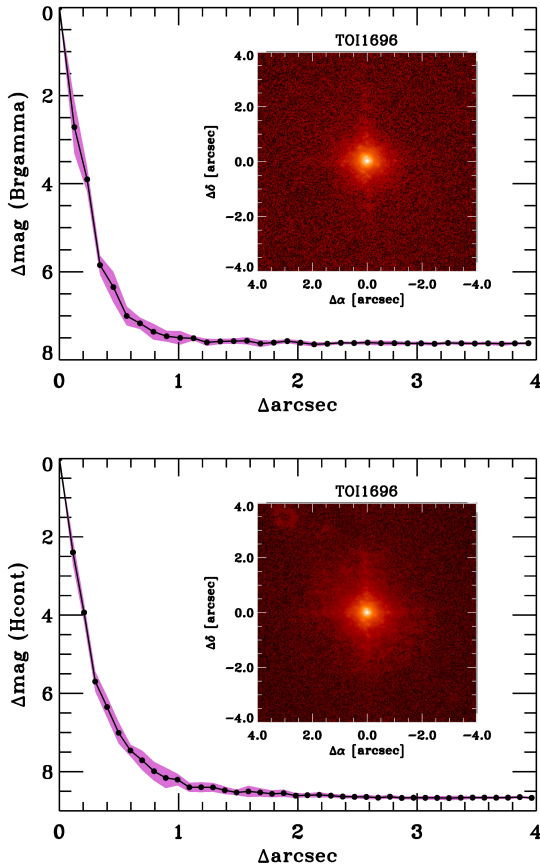
Figure 4. Palomar/PHARO images and contrast curves (top: Brγ; bottom: H$_{\rm cont}$) produced as described in Section 2.7.

088I and S21B-118I). The raw data were reduced using `IRAF` (Tody 1993) as well as a pipeline for the detector's bias processing and

wavelength calibrations developed by the IRD instrument team (Kuzuhara et al. 2018; Hirano et al. 2020). For the RV analyses and stellar parameter derivation, we computed a high-SNR coadded spectrum of the target following the procedures described in Hirano et al. (2020).

For use as a spectral template in the analysis described in Section 3.2, we also downloaded archival IRD data of GJ 699 (Barnard's Star)[7], which was obtained on 2019 March 23 (HST). We reduced and calibrated the GJ 699 data following the same procedures as the TOI-1696 data.

2.9. *Medium-resolution spectroscopy - IRTF/SpeX*

We collected observations of TOI-1696 on UT 2020 December 09 using SpeX, a medium-resolution spectrograph on the NASA Infrared Telescope Facility (IRTF) on Maunakea (Rayner et al. 2003). We obtained our observations in SXD mode with a $0''\!.3 \times 15''$slit, providing a spectral resolution of $R \approx 2000$ over a wavelength range 700 nm to 2550 nm. In order to remove sky background and reduce systematics, the spectra were collected using an ABBA nod pattern (with a separation of $7''\!.5$ between the A and B positions) and with the slit synced to the parallactic angle. We reduced our spectra using the `Spextool` reduction pipeline (Cushing et al. 2004) and removed

---

[7] Using the Subaru-Mitaka-Okayama-Kiso-Archive (SMOKA)

telluric contamination using `xtellcor` (Vacca et al. 2003). The derived spectra were used to calculate the stellar metallicity.

3. ANALYSES & RESULTS

3.1. *Stellar parameters estimation*

In the next subsections we estimate the fundamental stellar parameters of TOI-1696. First, the stellar effective temperature T_{eff} and metallicity [Fe/H] are derived from two independent methods; one is from the IRD spectra and the other is from the SpeX spectra and photometric relations. Second, the stellar radius $R_\star$, mass $M_\star$, and other related parameters are derived using empirical relations and the above T_{eff} and [Fe/H] values.

3.1.1. *Estimation of T_{eff} and [Fe/H]: from IRD spectra*

We derived the effective temperature T_{eff} and abundances of individual elements [X/H] from the coadded IRD spectrum. To avoid amplifying noise in the spectrum, we decided not to deconvolve the instrumental profile prior to these analyses.

We determined the parameters by the equivalent width comparison of individual absorption lines between the synthetic spectra and the observed ones. For T_{eff} estimation, 47 FeH molecular lines in the Wing-Ford band at $990 - 1020$ nm was used as same as in Ishikawa et al. (2022). We also derived the abundance of eight metal elements as described in Section A.1.

We iterated the T_{eff} estimation and the abundance analysis alternately until T_{eff} and metallicity were consistent with each other. First, we derived a provisional T_{eff} assuming solar metallicity ([Fe/H] = 0), and then we determined the individual abundances of the eight elements [X/H] using this provisional T_{eff}. Second, we redetermined T_{eff} adopting the iron abundance [Fe/H] as the input metallicity, and then we redetermined the abundances using the new T_{eff}. We iterated the estimation of T_{eff} and [Fe/H] until the final results and the results of the previous step agreed within the error margin. As a result, we derived $T_{\mathrm{eff}} = 3156 \pm 119$ K and [Fe/H] $= 0.333 \pm 0.088$ dex.

3.1.2. *Estimation of T_{eff} and [Fe/H]: from SpeX spectra and photometric relations*

Before analyzing our SpeX spectra, we corrected the data to the lab reference frame using `tellrv`[8] (Newton et al. 2014, 2022). We then determined metallicity with `metal`[9] (Mann et al. 2013), using only the K-band part of the spectrum, which is historically the most reliable, although the metallicities from H- and J-band are broadly consistent.

We calculated the stellar parameters using a series of photometric relations, following the Section 4.3 of (Dressing et al. 2019). First, we calculated the luminosity of the star using the Gaia EDR3 distance (Stassun & Torres 2021), 2MASS J magnitude, r magnitude (from the Carlsberg Meridian Catalogue; Muiños & Evans 2014), and the metallicity-dependent r-J bolometric correction in Table 3 of Mann et al. (2015). Next, we calculated the radius of the star using the relation between $R_\star$, absolute K magnitude, and [Fe/H] defined in Table 1 of Mann et al. (2015). Lastly, we calculated T_{eff} using the Stefan-Boltzmann law. As a result, we derived $T_{\mathrm{eff}} = 3207 \pm 99$ K and [Fe/H] $= 0.338 \pm 0.083$ dex.

The strong agreement in T_{eff} and [Fe/H] between the two methods suggests a high degree of reliability of the measurements. For the following analyses, we used the weighted mean of the two respective measurements for T_{eff} and [Fe/H], specifically, $T_{\mathrm{eff}} = 3185 \pm 76$ K and [Fe/H] $= 0.336 \pm 0.060$ dex.

3.1.3. *Estimation of stellar radius and mass*

We estimated other stellar parameters such as stellar mass $M_\star$, radius $R_\star$, surface gravity $\log g$, mean density $\rho_\star$, and luminosity $L_\star$ following the procedure described in Hirano et al. (2021). In short, the distributions of the stellar parameters are derived from a Monte Carlo approach using a combination of several empirical relations as well as the observed and literature values.

The $R_\star$ value was calculated through the empirical relation from Mann et al. (2015), and $M_\star$ from Mann et al. (2019). In deriving the stellar parameters by Monte Carlo simulations, we adopted Gaussian distributions for T_{eff} and [Fe/H] based on our spectroscopic analyses (see Sections 3.1.1 and 3.1.2), the apparent K_s-band magnitude from 2MASS, and the parallax from *Gaia* EDR3 (Stassun & Torres 2021). We

---

[8] https://github.com/ernewton/tellrv
[9] https://github.com/awmann/metal

Table 1. Main identifiers, equatorial coordinates, proper motion, parallax, optical and infrared magnitudes, and fundamental parameters of TOI-1696.

Parameter	Value	Source
Main identifiers		
TIC	470381900	TIC v8[a]
2MASS	J04210733+4849116	ExoFOP[a]
WISE	J042107.34+484911.5	ExoFOP[a]
UCAC4	695-028795	ExoFOP[a]
Gaia EDR3	270260649602149760	*Gaia* EDR3[b]
Equatorial coordinates, parallax, and proper motion		
R.A. (J2015.5)	$04^{\rm h}21^{\rm m}07.36^{\rm s}$	*Gaia* EDR3[b]
Dec. (J2015.5)	$+48°49'11.38''$	*Gaia* EDR3[b]
π (mas)	15.4752 ± 0.0345	*Gaia* EDR3[b]
μ_α (mas yr^{-1})	12.8726 ± 0.0345	*Gaia* EDR3[b]
μ_δ (mas yr^{-1})	-19.0463 ± 0.0269	*Gaia* EDR3[b]
Optical and near-infrared photometry		
TESS	13.9664 ± 0.00730068	TIC v8[a]
G	15.3056 ± 0.0028	*Gaia* EDR3[b]
$B_{\rm p}$	17.0511 ± 0.0051	*Gaia* EDR3[b]
$R_{\rm p}$	14.0457 ± 0.0039	*Gaia* EDR3[b]
B	18.467 ± 0.162	ExoFOP[a]
V	16.82 ± 1.133	ExoFOP[a]
J	12.233 ± 0.023	2MASS[c]
H	11.604 ± 0.031	2MASS[c]
Ks	11.331 ± 0.023	2MASS[c]
$W1$	11.134 ± 0.023	All*WISE*[d]
$W2$	10.984 ± 0.021	All*WISE*[d]
$W3$	10.71 ± 0.11	All*WISE*[d]
$W4$	$8.748\pm$	All*WISE*[d]
Fundamental parameters		
$T_{\rm eff}$ (K)	3185 ± 76	This work
$\log g$ (cgs)	4.959 ± 0.026	This work
[Fe/H] (dex)	0.336 ± 0.060	This work
$M_\star$ ($M_\odot$)	0.255 ± 0.0066	This work
$R_\star$ ($R_\odot$)	0.2775 ± 0.0080	This work
$\rho_\star$ (g cm^{-3})	$16.8^{+1.5}_{-1.4}$	This work
distance (pc)	65.03 ± 0.36	This work
Luminosity (L$_\odot$)	$0.00711^{+0.00083}_{-0.00075}$	This work

[a] https://exofop.ipac.caltech.edu/tess/
[b] Stassun & Torres (2021)
[c] Skrutskie et al. (2006)
[d] Cutri et al. (2021)

assumed zero extinction ($A_V = 0$), considering the proximity of the star to Earth.

As a result, we derived $R_\star = 0.2775 \pm 0.0080\ R_\odot$ and $M_\star = 0.255 \pm 0.0066\ M_\odot$ along with the other parameters listed in A.1. By interpolating Table 5 of Pecaut & Mamajek (2013) we determined the spectral type of TOI-1696 to be M4V (M3.9V $\pm$ 0.2).

To check the robustness of this analysis, we confirmed them to be in good agreement with stellar parameters derived through independent analyses based on SED fitting and ISOCHRONES (see Section A.2 and A.3).
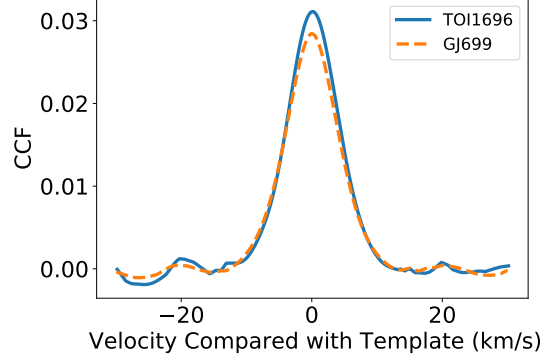
Figure 5. Calculated CCF of the IRD spectrum of TOI-1696 taken on 2021 January 30 at the orbital phase 0.247, to the template spectrum of GJ699, exhibiting a single peak with width 9.2 km s^{-1}. The dashed line shows the auto-correlation function of the GJ699 spectrum as a reference.

3.2. *Search for spectroscopic binary stars*

If a stellar companion orbits the target star, the observed spectra will generally be the combination of two stellar spectra with different radial velocities. To see if TOI-1696 is a spectroscopic binary (i.e. an SB2), we calculated the cross-correlation function (CCF) of the TOI-1696's IRD spectra with that of the well-known single-star GJ 699 (Barnard's Star). The spectrum of TOI-1696 used for the analysis was obtained on UT 2021 January 30 08:53, which corresponds to the an orbital phase of 0.247 based on the *TESS* ephemeris.

For the analysis, we divided the spectra into six wavelength bins that are less affected by telluric absorption: [988, 993 nm], [995, 1000 nm], [1009, 1014 nm], [1016, 1021 nm], [1023, 1028 nm], and [1030, 1033 nm]. We corrected the telluric absorption signal using the spectra of the rapid-rotator HIP 74625, which was observed at the same night. The CCF to the template spectrum was calculated for each segment, after barycentric velocity correction. Finally, we computed the median of the CCFs from each segment. As shown in Figure 5, the resulting CCF is clearly single-peaked. If the observed transit signals were actually caused by an eclipsing stellar companion, the RV difference at quadrature would be > 100 km s^{-1}, which would result in a second peak in the CCF given that the flux of such a companion would be detectable. We thus conclude TOI-1696 is not an eclipsing binary.

3.3. *Stellar age*

Because young stars are active and rapidly rotating, stellar activity and rotation period can be used as proxy for determining its youth. We did not find any stellar rotational signal in the *TESS* SPOC light curve, suggesting that the star is not very active. Similarly, no strong rotational signal was found in archival photometric data from ZTF Data Release 9 (Bellm et al. 2019; Masci et al. 2019) and ASAS-SN (Kochanek et al. 2017).

GJ 699 has a rotation period of 145 days and $v \sin i$ of less than 3 km s^{-1} (Toledo-Padrón et al. 2019), which is below the limit of IRD's resolving power ($\sim$70000, corresponding to $\sim$ 4.5 km s^{-1}). While the CCF of TOI-1696 has a FWHM value consistent with that of GJ 699 (see Figure 5), even if we assume the rotation axis of TOI-1696 is in the plane of the sky, relatively short rotation periods cannot be ruled out, as their rotational broadening would not be resolvable with IRD. However, fast rotation would most likely be accompanied with surface magnetic activity levels that would produce detectable photometric signals. We also used banyan Σ (Gagné et al. 2018) to check if TOI-1696 is a member of any known stellar associations, using its proper motion and the parallax from *Gaia* EDR3. banyan Σ tool[10] returned a value of 99.9% field star, suggesting it is not a member of any nearby young moving group. The non-detection by GALEX also means that the star is not young enough to be bright in the UV. We thus conclude that TOI-1696 is most likely a relatively old, slow rotator.

3.4. *Transit analysis*

We jointly fit the *TESS*, KeplerCam, Sinistro, MuSCAT3, and MuSCAT datasets using the PyMC3 (Salvatier et al. 2016), exoplanet[11] (Foreman-Mackey et al. 2019), starry (Luger et al. 2019), and celerite2 (Foreman-Mackey et al. 2017; Foreman-Mackey 2018) software packages. The model assumes a chromatic transit depth, a linear ephemeris, a circular orbit, and quadratic limb darkening. For efficient and uninformative sampling, the quadratic limb darkening coefficients were transformed

---

[10] http://www.exoplanetes.umontreal.ca/banyan/
[11] https://docs.exoplanet.codes/en/stable/

---

following Kipping (2013). To account for systematics in the ground-based datasets we included a linear model of airmass and other covariates, such as the pixel response function peak, width, and centroids, when available. To account for stellar variability and residual systematics in the *TESS* SPOC light curve, we included a Gaussian Process (GP Rasmussen & Williams 2005) model with a Matérn-3/2 covariance function. To account for the possibility of under- or over-estimated uncertainties, we included a white noise scale parameter for each dataset/band, enabling the errors to be estimated simultaneously with other free parameters; we placed Gaussian priors on these white noise scale parameters, with center and width equal to unity. We placed Gaussian priors on the stellar mass and radius based on the results in Table 1. We also placed Gaussian priors on the limb darkening coefficients based on interpolation of the parameters tabulated in Claret et al. (2012) and Claret (2017), propagating the uncertainties in the stellar parameters in Table 1 via Monte Carlo simulation.

To optimize the model we used the gradient-based BFGS algorithm (Nocedal & Wright 2006) implemented in scipy.optimize to find initial maximum a posteriori (MAP) parameter estimates. We then used these estimates to initialize an exploration of parameter space via "no U-turn sampling" (NUTS, Hoffman & Gelman 2014), an efficient gradient-based Hamiltonian Monte Carlo (HMC) sampler implemented in PyMC3.

Detailed plots showing the model fits to the ground-based datasets are shown in Figure 7, Figure 8, and Figure 9. We did not detect any significant wavelength dependence of the transit depth (see Figure 10), which rules out many plausible false positive scenarios involving eclipsing binaries (see Section 3.6 for more details). The results of this fit are listed in Table 2. Having established the achromaticity of the transit depth, we conducted a second fit with an achromatic model to robustly estimate the planet radius. This fit resulted in a final value of $R_P/R_\star = 0.1025 \pm 0.0014$, corresponding to an absolute radius of $3.09 \pm 0.11\ R_\oplus$, and all other parameters were unchanged.

3.5. *Companion mass constraints*

To put a limit on the mass of TOI-1696.01, we fit an RV model with a circular orbit to the RV

**Table 2.** Results of joint fit to the *TESS* and ground-based transit datasets.

Parameter	Value
Primary transit parameters	
$M_\star$ [$M_\odot$]	0.255 ± 0.007
$R_\star$ [$R_\odot$]	0.277 ± 0.008
T_0 [BJD]	$2458834.20115 \pm 0.00058$
P [days]	2.500311 ± 0.000004
$R_P/R_{\star,T}$	0.0952 ± 0.0062
$R_P/R_{\star,V}$	0.1021 ± 0.0057
$R_P/R_{\star,g}$	$0.1036^{+0.0060}_{-0.0068}$
$R_P/R_{\star,r}$	0.1053 ± 0.0034
$R_P/R_{\star,i}$	0.1023 ± 0.0020
$R_P/R_{\star,z}$	0.1026 ± 0.0020
$R_P/R_\star$	0.1025 ± 0.0014^a
b	$0.59^{+0.03}_{-0.04}$
Limb darkening parameters	
u_1 (T)	0.16 ± 0.01
u_2 (T)	0.48 ± 0.01
u_1 (V)	0.48 ± 0.02
u_2 (V)	0.30 ± 0.01
u_1 (g)	0.49 ± 0.01
u_2 (g)	0.31 ± 0.01
u_1 (r)	0.50 ± 0.01
u_2 (r)	0.25 ± 0.01
u_1 (i)	0.37 ± 0.01
u_2 (i)	0.28 ± 0.01
u_1 (z)	0.24 ± 0.01
u_2 (z)	0.36 ± 0.01
Derived parameters	
$R_{\rm p}$ [$R_\oplus$]	3.09 ± 0.11^a
a [AU]	0.0229 ± 0.0002
$T_{\rm eq}$ [K]	489 ± 13^b
T_{14} [hours]	1.00 ± 0.01

^{a}Derived from achromatic transit model fit.

^{b}Assuming a Bond albedo of 0.3.

data from Subaru/IRD. Between the *H*-band and the *YJ*-band spectra obtained with IRD, we opted to use the *H*-band spectra for RV analysis because of its higher SNR.[12] The data observed on 2021 January 29 was excluded be-

[12] There have been reports of unpredictable systematic errors caused by persistence light on the detector in *H*-band, especially when bright stars are observed before fainter stars. We checked the objects observed before TOI-1696 and found that none were more than 1.2 mag brighter in the *H*-band, i.e. persistence light isn't likely to be a problem with these data.
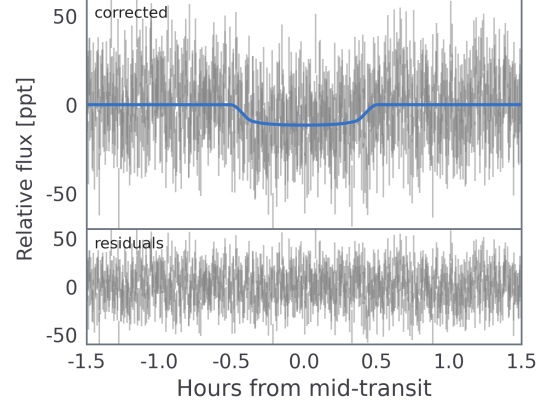
Figure 6. The phase-folded *TESS* light curve after removing the best-fit GP noise model, with the best-fit transit model (blue) from our joint analysis of the *TESS* and ground-based light curves.

cause of the possibility of an RV offset, as there was a gap of 8 months relative to the succeeding observations. We also removed any data with the clouds passing, which can cause systematic errors. The final dataset consisted of 9 RV measurements from 2021 September 29 to 2022 January 8.

We used the RV model included in PyTransit which we simplified to have five free parameters: phase-zero epoch T_0, period, RV semi-amplitude, RV zero point, and RV jitter term. For the T_0 and the period, we put Gaussian priors using the T_0 and period derived from the transit analysis. For the other parameters we put wide uniform priors. We ran the built-in Differential Evolution optimizer and then sample the parameters with Markov Chain Monte Carlo (MCMC) using 30 walkers and 10^4 steps. We use the following equation to derive the planet mass,

$$M_p = \left(\frac{PM_s^2}{2\pi}\right)^{1/3} \frac{K(1-e^2)^{1/2}}{\sin(i)} \qquad (1)$$

where $M_{\rm p}$ is planet mass, $M_\star$ is star mass, P is orbital period, K is RV semi-amplitude, e is eccentricity (fixed to zero), and i is inclination (fixed to $90°$). To propagate uncertainties, we use the posteriors for $M_\star$ and P from previous analyses.

In Figure 11 we plot Keplerian orbital models corresponding to different masses encompassing the $68^{\rm th}$, $95^{\rm th}$, and $99.7^{\rm th}$ percentiles of the semi-amplitude posterior distribution. The $2\text{-}\sigma$ upper limit is 48.8 $M_\oplus$ which places the companion 2 orders of magnitude below the
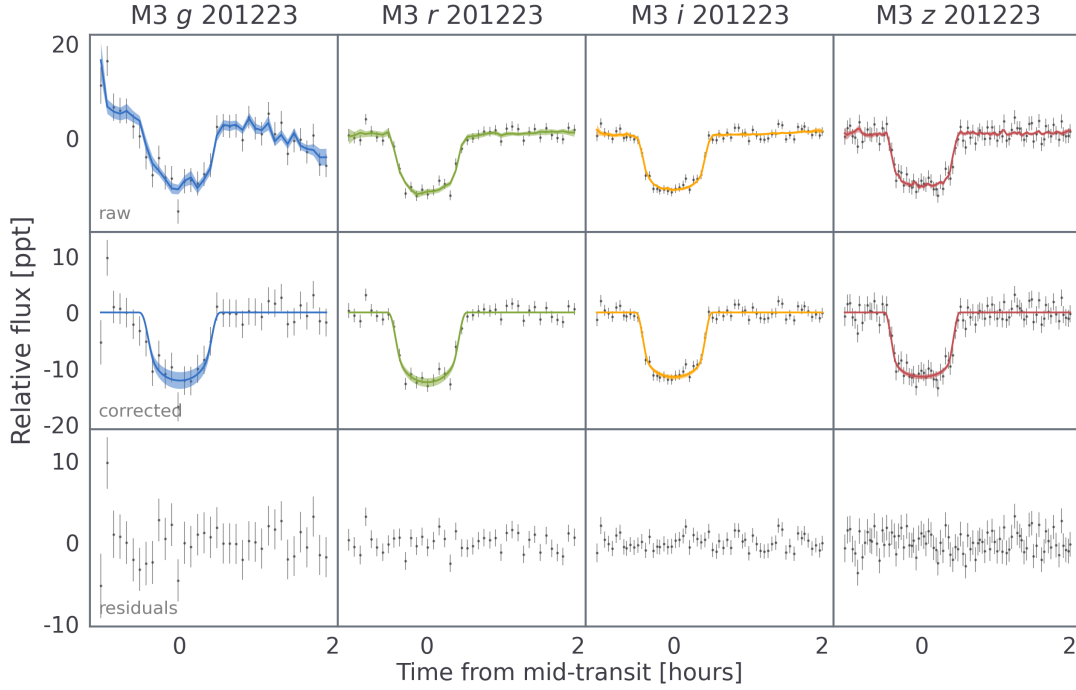
Figure 7. Transit model fit to the MuSCAT3 (M3) data from 2020 December 23, ordered column-wise per bandpass. The top row shows the raw data with the transit and systematics model, the middle row shows the systematics-corrected data with only the transit model, and the bottom row shows the residuals from the fit. The colors of the model correspond to the photometric bandpass of each dataset; see also Figure 10.
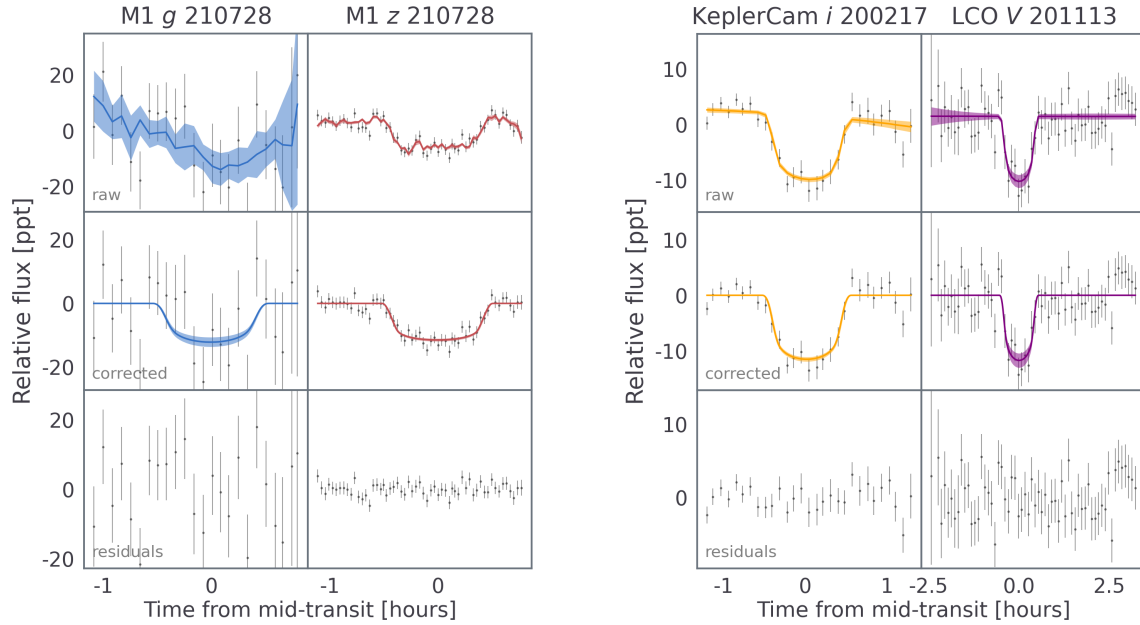
Figure 8. Same as Figure 7, but for the MuSCAT (M1) data from 2021 July 28.

Figure 9. Same as Figure 7, but for the Kepler-Cam and LCO data from 2020 February 17 and 2021 November 13, respectively.

deuterium burning mass limit. The best-fit semi-amplitude is $K = 14.4\,\mathrm{ms}^{-1}$, which corresponds to a mass of $M_p = 12.3 M_\oplus$, and the best-fit jitter value is $\sigma_K = 62\ \mathrm{m\,s}^{-1}$.
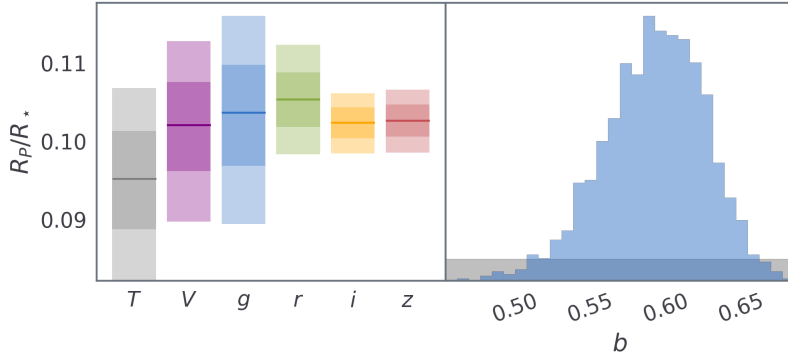
Figure 10. Posteriors of the planet-to-star radius ratio ($R_P/R_\star$) in each bandpass (left) and impact parameter (right) from the joint fit to the *TESS* data and the ground-based data shown in Figure 7, Figure 8, and Figure 9; the gray shaded region in the right panel represents the uniform prior used in the fit, while the blue histogram is the posterior.

We calculated an expected planetary mass of ~ 8 $M_\oplus$ with MRExo[13], which uses a mass-radius relationship calibrated for planets around M dwarfs (Kanodia et al. 2019). This mass corresponds to a semi-amplitude of $9.4\mathrm{m\,s^{-1}}$, but the observed RV data exhibits significantly larger variability ($\sigma \approx 52\mathrm{m\,s^{-1}}$). We interpret this variability as being responsible for the large jitter value found by the fit, which suggests it is out-of-phase with TOI-1696.01. Since the star appears to be quiet, one explanation for this signal is the existence of an additional (possibly non-transiting) planet, but more RV measurements would be required to determine if this is the case. Furthermore, if such a planet were dynamically interacting with TOI-1696.01, then this could help explain TOI-1696.01's location in a sparsely populated part of the period-radius plane (see Section 4).

3.6. *Eliminating false positive scenarios*

A number of astrophysical scenarios can mimic the transit signal detected from *TESS* photometry, including an eclipsing binary (EB) with a grazing transit geometry, a hierarchical EB (HEB), and a diluted eclipse of a background (or foreground) EB (BEB) along the line of sight of the target. In the following, we will examine the plausibility of each scenario.

First, the Renormalised Unit Weight Error (RUWE) from *Gaia* EDR3 is 1.12, which suggests that TOI-1696 is single (Belokurov et al. 2020). We can also rule out the EB scenario based on the analysis of the IRD CCF in Section 3.2, and the mass constraint derived in
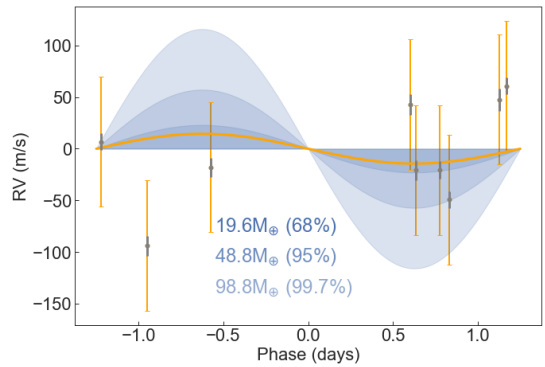
Figure 11. Phase-folded RVs with Keplerian models corresponding to the 1-, 2-, and 3-σ mass upper limits. Gray points with the error bars show the errors estimated from the data processing method described in Section 2.8. The error bars in orange show the original errors + jitter term value of $62~\mathrm{m\,s^{-1}}$ (added in quadrature) from the best-fit RV model (orange line, best $\mathrm{M_p} = 12.3 M_\oplus$.)

Section 3.1.1. Finally, the absence of any wavelength dependence of the transit depth from our chromatic transit analysis (Section 3.4) is incompatible with contamination from a star of different spectral type (colour) than the host star, the details of which are discussed in the Appendix B. In the absence of dilution, the measured radius of 3.09 ± 0.11 $R_\oplus$ (0.27 R_Jup) equals the true radius, which makes it significantly smaller than the lower limit of 0.8 R_Jup expected for brown dwarfs (Burrows et al. 2011).

Grazing transit geometries can also be eliminated, as the impact parameter is constrained to $b < 0.7$ at the 99% level based on our transit and contamination analyses. The apparent boxy shape of our follow-up lightcurves is in

stark contrast with the V-shaped transit expected for grazing orbits. Hence, grazing EB scenario is ruled out.

Moreover, we can constrain the classes of HEBs that can reproduce the observed transit depth and shape using our multi-band observations. We aim to compute the eclipse depths for a range of plausible HEBs in the bluest and reddest bandpasses where they are expected to vary significantly. We adopt the method presented in Bouma et al. (2020) to perform the calculation taking into account non-zero impact parameter, the details of which are discussed in the Appendix C. Comparing the simulated eclipse depths with the observed depth in each band, we found that there is no plausible HEB configuration explored in our simulation that can reproduce the observed depths in multiple bands simultaneously. Hence, the HEB scenario is ruled out.

Although, TOI-1696's probability of being a BEB is very high a priori given its location at the galactic plane, we argue in the following that the BEB scenario is extremely unlikely.

Our MuSCAT3 observation can resolve the signal down to 3″, which represents the maximum radius within which the signal must originate. Furthermore, our high-resolution speckle imaging ruled any nearby star and blended sources down to 0.1″ at a delta mag of 4.5. We checked archival images taken more than 60 years apart, but the proper motion of TOI-1696 is not enough to obtain a clear view along the line of sight of the star. However, we can use statistical arguments to estimate the probability of a chance-aligned star. To do this, we use the population synthesis code TRILE-GAL[14] (Girardi et al. 2005), which can simulate the Galactic stellar population along any line of sight. Given the position of TOI-1696, we found a probability of 5×10^{-8} to find a star brighter than $T=16$[15], within an area equal to the smallest MuSCAT3 photometric aperture (aperture radius = 3″). Assuming all such stars are binary and preferentially oriented edge-on to produce eclipses with period and depth consistent with the *TESS* detection,

then this can represent a very conservative upper limit of a BEB scenario. Despite the small probability of a BEB based on the trivial star counting argument, we discuss relevant tools in the following section for a more thorough statistical modeling.

3.7. *Statistical validation*

Here we quantify the false positive probability (FPP) of TOI-1696.01 using the Python package VESPA and TRICERATOPS (Morton 2015; Giacalone & Dressing 2020), the details of which are discussed in Section D. Although we were able to rule out the classes of EB, BEB, and HEB in Section 3.6, we ran VESPA considering all these scenarios for completeness and computed a formal FPP$< 1 \times 10^{-6}$ which robustly quantifies TOI-1696.01 as a statistically validated planet. Additionally, we validated TOI-1696.01 using TRICERATOPS and found FPP=0.0020. Giacalone et al. (2021) noted that TOIs with FPP < 0.015 have a high enough probability of being bona fide planets to be considered validated. The low FPPs calculated using VESPA and TRICERATOPS added further evidence to the planetary nature of TOI-1696.01. We now refer to the planet as TOI-1696 b in the remaining sections.

4. DISCUSSION

4.1. *The nature of the planet*

Here, we consider the nature of TOI-1696 b by placing it in context with the population of known exoplanets[16]. Figure 12 shows a radius vs period diagram, indicating that there are only a handful of planets with similar characteristics to TOI-1696 b. The measured planetary radius $R_{\rm p}$ of 3.09 ± 0.11 $R_\oplus$ and the orbital period P of 2.50031 ± 0.00001 days, places it securely within the bounds of the Neptunian desert as defined by Mazeh et al. (2016). The region occupied by TOI-1696 remains sparsely populated despite recent discoveries of *TESS* planets within the Neptunian desert (e.g. Murgas et al. 2021; Brande et al. 2022).

It should be noted that the Neptunian desert was originally determined based on a population of planets orbiting mainly solar-type stars

---

[14] http://stev.oapd.inaf.it/cgi-bin/trilegal

[15] T denotes the *TESS* bandpass. The maximum delta magnitude was computed using dT=-2.5log$_{10}$(depth), which translates to the magnitude that can produce a 100% eclipse

[16] Based on a query of the NASA Exoplanet Archive "Confirmed Planets" table on 2022 January 31, https://exoplanetarchive.ipac.caltech.edu/
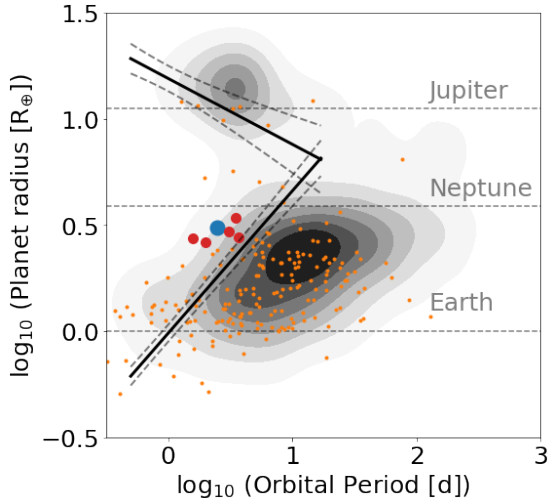
Figure 12. TOI-1696 b (blue) in the context of known transiting planets (contours). TOI-1696 b appears to be within or close to the boundaries of the Neptunian desert (solid black lines) in the period-radius plane defined by Mazeh et al. (2016). The dashed lines refer to the boundaries' uncertainty regions. The orange points indicate planets orbiting M dwarfs ($T_{\rm eff} < 3800$K) and the red points indicate the five planets most similar in this parameter space to TOI-1696 b: K2-25 b, K2-320 b, GJ 1214 b, TOI-269 b, and TOI-2406 b.

from the *Kepler* mission. Because TOI-1696 is an M dwarf, the incident flux at a given orbital separation will be less than solar-type stars. Nevertheless, we emphasize that the target exists in a sparsely populated region of parameter space, despite the large number of planets discovered around M dwarfs since the *Kepler* mission (i.e. from *K2* and *TESS*). For example, if we limit the comparison to the 279 confirmed planets around M dwarfs with $T_{\rm eff}$ below 3800 K, only 14 planets have been found so far with orbital periods shorter than 10 days and planetary radii in the range $2.5R_\oplus < R_{\rm p} < 5~R_\oplus$. As shown in Figure 12, TOI-1696 b is similar to K2-25 b(Mann et al. 2016), K2-320 b(Castro González et al. 2020), GJ 1214 b(Charbonneau et al. 2009), TOI-269 b(Cointepas et al. 2021), and TOI-2406 b(Wells et al. 2021) in terms of orbital period and radius. In particular, TOI-2406 b appears most similar to TOI-1696 b as it orbits around a mid-M dwarf with an effective temperature of 3100 ± 75, and has a radius of $2.94 \pm 0.17~R_\oplus$ and orbital period of 3.077 days. TOI-2406 is also thought to be relatively old without any activity signal. As both TOI-1696 b and TOI-2406 b are excellent targets for

detailed characterization studies, together they may provide unique insights into this class of planet. There is also some similarity between TOI-1696 b and the Neptunian Desert planets orbiting young host stars, such as AU Mic b and c, K2-25 b, K2-95 b and K2-264 b. It has been suggested that these planets may have inflated radii and could possibly still be undergoing atmospheric mass-loss (e.g. Mann et al. 2016). Further study of TOI-1696 b could reveal whether its similarity to these planets (despite being older) is only superficial, or if it is indicative of an inflated radius.

### 4.2. *Prospects for transmission spectroscopy*

Given the rarity of this planet, it would be useful to assess its prospects for future atmospheric observations to understand its formation and evolution. In particular, the relatively large size of the planet compared to its host star makes it a good candidate for transmission spectroscopy. Using Equation 1 in Kempton et al. (2018), we calculated the transmission spectroscopy metric (TSM) of TOI-1696 b from its mass, radius, equilibrium temperature, stellar radius, and J-band magnitude. We used the values in Figure 1 and 2, and assumed a mass of 8 $M_\oplus$ estimated by MRExo. The derived TSM value of TOI-1696 b is 105.6. For reference, Kempton et al. (2018) suggested that planets with TSM>90 are ideal targets for atmospheric follow-up.

For comparison, we calculated the TSM for the known population of transiting M dwarf planets. We selected planets with $T_{\rm eff} < 3800$K, $R_{\rm p} < 10R_\oplus$, and H < 11mag[17]. For planets without mass measurements, we assumed the masses predicted by MRExo. For planets without an equilibrium temperature, we estimated it from the semi-major axis and the host star's effective temperature (assuming zero albedo). Figure 13 shows the computed TSM values for the selected samples of planets. The TSM of TOI-1696 b places it in the top 10, making it one of the best targets for future atmospheric investigations.

4.3. *Existence of a primordial atmosphere*

Up to this point in the section, the discussion has been based on the assumption that

---

[17] Based on a query of the NASA Exoplanet Archive Confirmed Planets table as of 2022 January 31
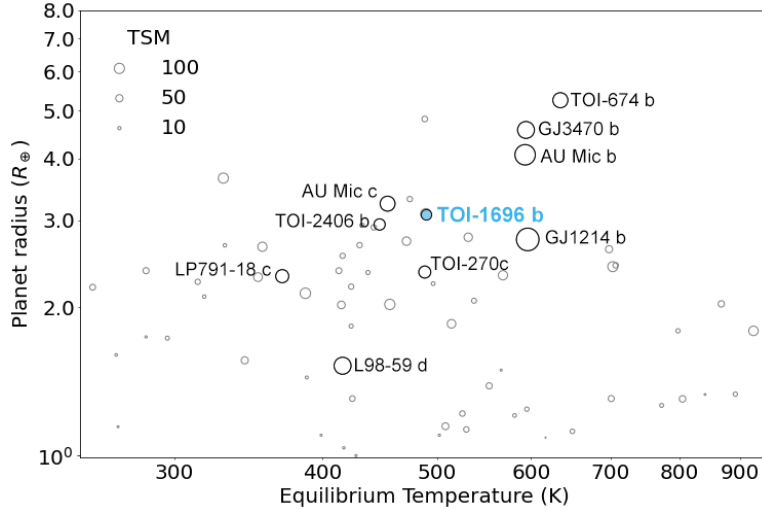
Figure 13. Planetary equilibrium temperature vs radius for TOI-1696 b and other planets with $Rp < 10R_\oplus$, with the host stars having $T_{\text{eff}} < 3800$K and $H < 11$mag. The point size represents the calculated TSM values. Data points with a planet name beside them are those with a higher TSM values than the target.
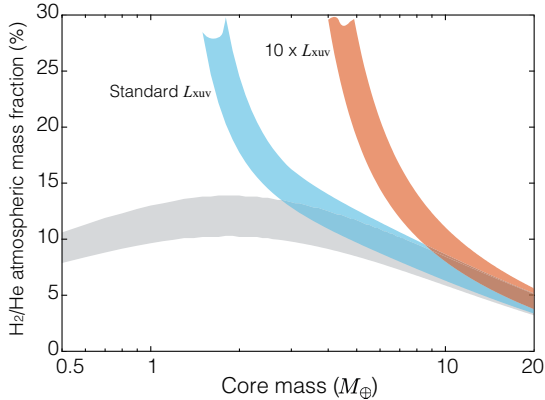
Figure 14. Initial H_2/He atmospheric mass fraction of a TOI-1696 b-like planet that satisfies the radius of 3.09 ± 0.11 $R_\oplus$ and $T_{\text{eq}} = 489 \pm 13$ K after photo-evaporative mass loss for 8 Gyr under the standard XUV radiation field (L_{XUV}) and $10L_{\text{XUV}}$. The grey region shows the H_2/He atmospheric mass fraction that reproduces the observed radius of TOI-1696 b with a rocky core.

the target has an atmosphere. Usually it is thought that planets above the so-called radius gap can retain their atmospheres (Weiss & Marcy 2014; Rogers 2015). However, does TOI-1696 b actually have an H_2/He atmosphere? Here we study the atmospheric mass that TOI-1696 b can retain after $\sim$ 8 Gyr under a stellar XUV irradiation. The mass of TOI-1696 b remains poorly constrained as discussed in Section 3.5. We modeled TOI-1696 b as a rocky planet with Earth-like core compositions (MgSiO$_3$:Fe = 7:3) in the mass range from $0.5M_\oplus$ to $20M_\oplus$. The silicate man-

tle and iron core were described by the 3rd-order Birch-Murnagham EoS for MgSiO$_3$ perovskite (Karki et al. 2000; Seager et al. 2007) and the Vinet EoS for ϵ-Fe (Anderson et al. 2001), respectively. The Thomas-Fermi Dirac EoS (Salpeter & Zapolsky 1967) was applied to high-pressure EoS for MgSiO$_3$ at $P \geq 4.90$ TPa and Fe at $P \geq 2.09 \times 10^4$ GPa (Seager et al. 2007; Zeng & Sasselov 2013). The pressure and temperature in a H_2/He envelope were calculated using the SCvH EoS (Saumon et al. 1995).

We computed the thermal evolution of TOI-1696 b with a H_2/He atmosphere by calculating its interior structure in hydrostatic equilibrium for $\sim$ 8 Gyr, and calculated its mass loss process. The initial mass fraction of a H_2/He atmosphere for a rocky planet ranges from 0.001% to 30% of its core mass. The energy-limited hydrodynamic escape (Watson et al. 1981) controls the mass loss rate given by

$$\frac{dM_{\text{p}}}{dt} = -\eta \frac{R_{\text{p}}^3 L_{\text{XUV}}(t)}{4GM_{\text{p}}a^2 K_{\text{tide}}}, \qquad (2)$$

η is the heating efficiency due to stellar XUV irradiation, L_{XUV} is the stellar XUV luminosity, G is the gravitational constant, and R_{p} is the planetary radius (Erkaev et al. 2007). Since the heating efficiency for a hydrogen-rich upper atmosphere was lower than 20 % (Shematovich et al. 2014; Ionov & Shematovich 2015), we adopted $\eta = 0.1$. K_{tide} is the reduction factor of a gravitational potential owing to the

effect of a stellar tide:

$$K_{\mathrm{tide}}(\xi) = 1 - \frac{3}{2\xi} + \frac{1}{2\xi^3} < 1, \quad \xi = \frac{R_{\mathrm{H}}}{R_{\mathrm{p}}}, \quad (3)$$

where R_{H} is the Hill radius. The XUV luminosity (L_{XUV}) of TOI-1696 followed from the X-ray-to-bolometric luminosity relations of M-type stars (Jackson et al. 2012), where we adopted the current luminosity of TOI-1696 as its bolometric luminosity. We also considered a $10L_{\mathrm{XUV}}$ model because of the large uncertainty in L_{XUV} of young M dwarfs.

Figure 14 shows the initial H_2/He atmosphere of a TOI-1696 b-like planet that reproduces the radius of 3.09 ± 0.11 $R_{\oplus}$ at the current location (i.e., $T_{\mathrm{eq}} = 489 \pm 13$ K) after the mass loss driven by the standard XUV radiation (L_{XUV}: blue) and 10 times higher one ($10L_{\mathrm{XUV}}$: red). The grey region shows the H_2/He atmospheric mass fraction of TOI-1696 b with a rocky core that satisfies its observed radius. The observed radius of TOI-1696 b favors the existence of a H_2/He atmosphere atmosphere with $\gtrsim 3$ wt% unless its core contains icy material. We find that TOI-1696 b can possess the H_2/He atmosphere for 8 Gyr if its core mass is larger than $\sim 1.5 M_{\oplus}$ ($\sim 4 M_{\oplus}$ for $10L_{\mathrm{XUV}}$ models). If TOI-1696 b initially had the H_2/He atmosphere of $\lesssim 3\%$, it should be completely lost. Also, TOI-1696 b with mass of $\gtrsim 10 M_{\oplus}$ can retain almost all the H_2/He atmosphere accreted from a disk. These suggest that TOI-1696 b with a rocky core of $\gtrsim 1.5 - 4 M_{\oplus}$ is likely to be a sub-Neptune with a H_2/He atmosphere.

5. CONCLUSIONS

TESS found transit signals of a sub-Neptune planet orbiting a mid-M dwarf TOI-1696. To validate and characterize the planetary system, we conducted follow-up observations of this system including ground-based transit photometry, high-resolution imaging, and high- and medium-resolution spectroscopy.

We have used several methods to determine the stellar parameters based on the results of the spectroscopic observations, and have confirmed that the results are consistent. The host star, TOI-1696, is a M-type star with a $M_{\star}$ at 0.255 ± 0.0066 $M_{\odot}$ and T_{eff} at 3185 ± 76 K.

The fact that this target is located near the Galactic plane makes validation difficult. We used the results obtained to rule out various scenarios that could reproduce the *TESS* signal (grazing EB, HEB, and BEB).

The validated planet, TOI-1696 b is a Sub-Neptune size planet with the radius at 3.09 $R_{\oplus}$ and rotation period at 2.5 days, which locates in the Neptunian desert. To see its atmospheric properties, we calculated how much of the atmosphere it currently retains, and found the planet likely to retain the H_2/He atmosphere if it has a core of > 1.5–$4 M_{\oplus}$. In order to statistically evaluate the feasibility of transmission spectroscopy on this planet, we have also calculated and compared the TSM and concluded that this target is one of the planets with the best prospects for atmospheric detection among the currently known Sub-Neptune-sized planets. In addition, future RV observations with high-resolution infrared spectrographs such as IRD will allow us to place more substantial limits on the planetary mass.

Japan, and at the Gemini North telescope, located within the Maunakea Science Reserve and adjacent to the summit of Maunakea. We are honored and grateful for the opportunity of observing the Universe from Maunakea, which has cultural, historical, and natural significance in Hawaii. Our data reductions benefited from PyRAF and PyFITS that are the products of the Space Telescope Science Institute, which is operated by AURA for NASA. This research made use of Astropy,[18] a community-developed core Python package for Astronomy (Astropy Collaboration et al. 2013, 2018). Some of the observations in the paper made use of the High-Resolution Imaging instrument(s) 'Alopeke. 'Alopeke was funded by the NASA Exoplanet Exploration Program and built at the NASA Ames Research Center by Steve B. Howell, Nic Scott, Elliott P. Horch, and Emmett Quigley. 'Alopeke (and/or Zorro) was mounted on the Gemini North (and/or South) telescope of the international Gemini Observatory, a program of NSF's NOIRLab, which is managed by the Association of Universities for Research in Astronomy (AURA) under a cooperative agreement with the National Science Foundation. on behalf of the Gemini partnership: the National Science Foundation (United States), National Research Council (Canada), Agencia Nacional de Investigación y Desarrollo (Chile), Ministerio de Ciencia, Tecnología e Innovación (Argentina), Ministério da Ciência, Tecnologia, Inovações e Comunicações (Brazil), and Korea Astron-

APPENDIX

A. DETAILED METHODS OF STELLAR PARAMETER ESTIMATION

A.1. *Abundances of eight metal elements from IRD spectra*

We calculated the abundances of seven other elements other than iron from IRD spectra. We used 28 lines in total caused by neutral atoms of Na, Mg, Ca, Ti, Cr, Mn, and Fe and singly ionized Sr. The detailed procedures of abundance analysis and error estimation are described in Ishikawa et al. (2020). Figure A.15

shows the final values of abundance after the iteration. From the final values of the abundances of the eight elements, [M/H] was determined by calculating the average weighted by the inverse of the square of their estimated errors.

A.2. *Estimation of Stellar Radius and Mass: SED Fitting*

As an independent determination of the basic stellar parameters, we performed an analysis of the broadband spectral energy distribution (SED) of the star together with the *Gaia* EDR3 parallax (Stassun & Torres 2021), in order to determine an empirical measurement of

[18] http://www.astrop.org
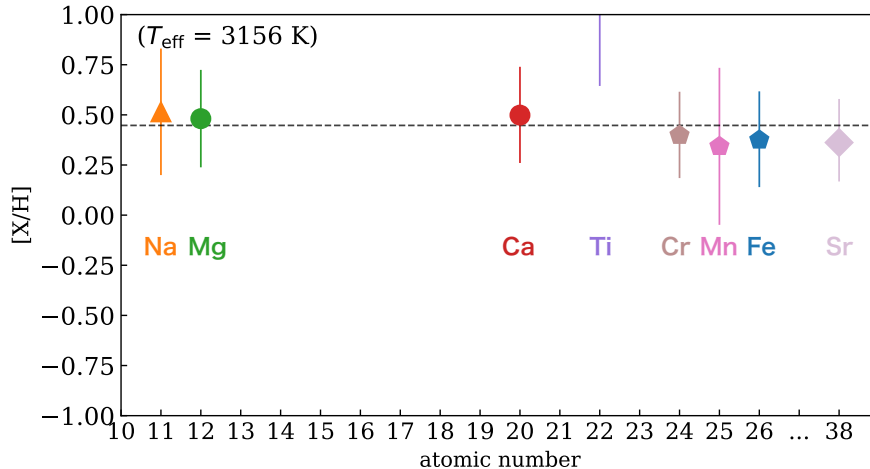
Figure A.15. Metallicity values derived from IRD spectrum. The horizontal dashed line corresponds to the weighted average [M/H].

the stellar radius, following the procedures described in Stassun & Torres (2016); Stassun et al. (2017, 2018). We pulled the JHK_S magnitudes from *2MASS*, the W1–W3 magnitudes from *WISE*, and the *grizy* magnitudes from Pan-STARRS. Together, the available photometry spans the full stellar SED over the wavelength range 0.4–10 μm (see Figure A.16).

We performed a fit using NExtGen stellar atmosphere models, with the effective temperature ($T_{\rm eff}$) and metallicity ([Fe/H]) constrained from the spectroscopic analysis. The remaining free parameter is the extinction A_V, which we fixed at zero due to the star's proximity. The resulting fit (Figure A.16) has a reduced χ^2 of 1.7. Integrating the (unreddened) model SED gives the bolometric flux at Earth, $F_{\rm bol} = 5.20 \pm 0.25 \times 10^{-11}$ erg s^{-1} cm^{-2}. Taking the $F_{\rm bol}$ and $T_{\rm eff}$ together with the *Gaia* parallax, gives the stellar radius, $R_\star = 0.276 \pm 0.015$ R$_\odot$. We used the $T_{\rm eff}$ and [Fe/H] values from spectroscopic results as priors for the parameter estimation.

In addition, we estimated the stellar mass from the empirical relations of Mann et al. (2019), giving $M_\star = 0.279 \pm 0.014$ M$_\odot$. Finally, the radius and mass together imply a mean stellar density of $\rho_\star = 18.79 \pm 3.26$ g cm^{-3}.

A.3. *Stellar parameter comparison*

In addition to the methods described above, we used the Python package ISOCHRONES, which calculates stellar parameters from the stellar evolution models. The three methods are not fully independent, as some of them use
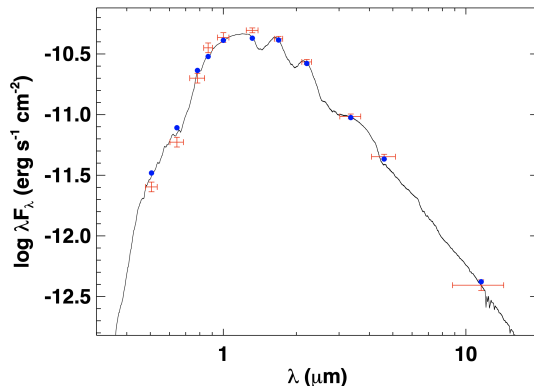
Figure A.16. Spectral energy distribution of TOI-1696. Red symbols represent the observed photometric measurements, where the horizontal bars represent the effective width of the passband. Blue symbols are the model fluxes from the best-fit NextGen atmosphere model (black).

the same relations such as mass derivation from Mann et al. (2019), but comparing three results are useful to confirm the results are robust. The derived stellar parameters agreed within $1 \sim 2\sigma$, as shown in A.1. We pick up the results from the empirical relations as our final stellar parameters in Table 1.

B. CONTAMINATION ANALYSIS

Contamination leads to a decrease in the observed transit depth (the planet appears to be smaller than it truly is), and this effect is achromatic even if the host and the contaminant(s) are of different spectral types. Having simultaneous multicolor photometry allows us to measure possible contamination and consequently

Table A.1. Stellar parameters which were derived from empirical relations (Method 1; Section 3.1.3), SED fitting (Method 2; Section A.2) and ISOCHRONES (Method 3;Section A.3). [†]The resulting posterior is approximately zero and non-Gaussian as a result of using a tight uniform prior close to 0 for numerical reasons.

Parameter	Method 1	Method 2	Method 3
$T_{\rm eff}$ (K)	-	3130 ± 75	3159 ± 40
[Fe/H] (dex)	-	0.2 ± 0.3	$0.232^{+0.035}_{-0.038}$
$M_\star$ ($M_\odot$)	0.255 ± 0.0066	0.279 ± 0.014	$0.276^{+0.006}_{-0.005}$
$R_\star$ ($R_\odot$)	0.2775 ± 0.0080	0.280 ± 0.014	0.291 ± 0.005
$\log g$ (cgs)	4.959 ± 0.026	4.990 ± 0.049	$4.955^{+0.008}_{-0.007}$
$\rho_\star$ (g cm^{-3})	$16.8^{+1.5}_{-1.4}$	18.0 ± 2.9	$16.282^{+0.598}_{-0.617}$
distance (pc)	65.03 ± 0.36	-	$65.390^{+0.540}_{-0.464}$
Luminosity ($L_\odot$)	$0.00711^{+0.00083}_{-0.00075}$	-	-
A_V (mag)	0 (fixed)	0 (fixed)	$\sim 0^\dagger$
F_{bol} (cgs)	-	$5.19(18) \times 10^{-11}$	-
$M_K s$ (mag)	7.265 ± 0.026	-	-

provides strong constraints on the false positive scenarios discussed in Section 3.6.

Following the methods presented in Parviainen et al. (2020, 2021), we used the physics-based contamination model included in Py-Transit v21 to model the light curves using a transit model that includes a light contamination component based on model stellar spectra leveraging multicolor photometry. Fitting the transit+contamination model to MuSCAT3 lightcurves allows us to measure the contamination in i-band[19], the effective temperature of the host ($T_{\rm eff,H}$), and the effective temperature of the contaminant ($T_{\rm eff,C}$).

We used normal priors for the period and T_0 based on the results of our transit analysis. We also used normal priors on limb darkening, host effective temperature, and host star density, based on our spectroscopic analysis. Among them, the spectroscopic priors are the most important. Without a limb darkening prior, the transit fit in g-band is boxy perhaps due to the sparse data sampling. Without the $T_{\rm eff,H}$ prior, the posteriors are not well behaved. Without the host $\rho_\star$ prior, the model converges to very high values (~ 33g cm^{-3}) which is inconsistent with the results from our previous analyses.

The joint and marginal posteriors of the relevant parameters are shown in Figure B.1. Significant levels of blending from sources with effective temperature different from that of the host star are excluded, and also the blending

from sources with $T_{\rm eff,C} \sim T_{\rm eff,H}$ are strongly constrained.

C. HEB SIMULATION

We assumed that each system was composed of the primary star (TOI-1696, Star 1), plus a tertiary companion (Star 3) eclipsing a secondary companion (Star 2) every 2.5 d. For a grid of secondary and tertiary star masses ranging from 0.1 to $0.4 M_\odot$, we then calculated the observed maximum eclipse depth caused by Star 3 eclipsing Star 2 in MuSCAT3 g- and z-bands using the following procedure. First, we interpolated $L_\star$ and $T_{\rm eff}$ of Star 2 and Star 3 from MIST isochrones given their masses, and the age, metallicity, and mass of Star 1 in Table 1. We then computed the blackbody function of each star given their $T_{\rm eff}$ then convolved it with the transmission functions for each band downloaded from the SVO filter profile service[20]. We then integrated the result using the trapezoidal method and computed the bolometric flux $F_{\rm bol}$, using the integrated functions above. Using Stefan-Boltzmann law and given $T_{\rm eff}$ and $L_\star$, we computed the component radii and luminosities to derive the eclipse depth.

Figure C.2 shows the HEB configurations that produce eclipse depths in g- (blue) and z-bands (red) that are consistent with the observed depth for two given impact parameters. The lower impact parameter corresponds to the 3-σ lower limit derived from our contamina-

---

[19] We adopt i as reference passband for simplicity

[20] http://svo2.cab.inta-csic.es/theory/fps/
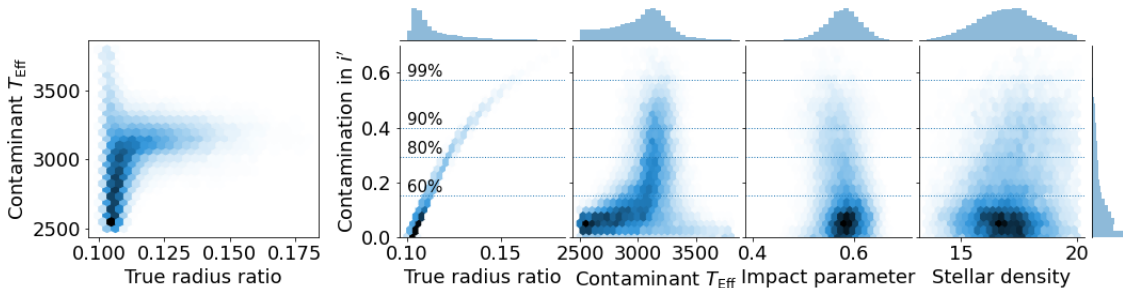
Figure B.1. Joint and marginal posteriors for the key parameters from the transit+contamination modelling of the MuSCAT3 multicolor light curves. Contamination due to sources with significantly different effective temperature than the host is ruled out.

tion analysis while the other impact parameter corresponds to the median value derived in our transit analysis. We confirm that indeed eclipses of an HEB are always deeper in the red than in the blue bands (i.e higher m_2/m_1 in z- than g-band) since the eclipsing companions are usually redder than the central star. The important point here is that the HEB configurations that produce eclipses consistent with our observation do not overlap within 1-σ in g- and z-bands for any reasonable impact parameters. Note also that our contamination analysis constrained possible contaminants to have the same colour as the host star, so only masses very close to TOI-1696 (vertical dashed line in Figure C.2) are allowed. Thus, we can rule out the HEB false positive scenario.

D. VALIDATION WITH VESPA AND TRICERATOPS

VESPA[21] was originally developed as a tool for statistical validation of planet candidates identified by the *Kepler* mission (e.g. Morton et al. 2016), but has also been used extensively to validate planets from subsequent missions, such as *K2* (e.g. Livingston et al. 2018; de Leon et al. 2021). VESPA compares the likelihood of a planetary scenario to the likelihoods of several astrophysical false positive scenarios involving eclipsing binaries (EBs), hierarchical triple systems (HEBs), background eclipsing binaries (BEBs), and the double-period cases of all these scenarios. The likelihoods and priors for each scenario are based on the shape of the transit signal, the star's location in the Galaxy, and single-, binary-, and triple-star model fits to the observed photometric and spectroscopic properties of the star generated

using ISOCHRONES. We used the MuSCAT3 lightcurve because of its high SNR and low levels of limb darkening, which provides the best constraint on the transit shape. We also used the Gemini and Palomar contrast curves described in Section 2.6, a maximum aperture radius of `maxrad` $=3''$(interior to which the transit signal must be produced), and ran the simulation using a population size of n=10^6, resulting to a formal FPP$< 1 \times 10^{-6}$.

We also used TRICERATOPS[22] which is a tool developed to validate TOIs (Giacalone & Dressing 2020; Giacalone et al. 2021) by calculating the Bayesian probabilities of the observed transit originating from several scenarios involving the target star, nearby resolved stars, and hypothetical unresolved stars in the immediate vicinity of the target. These probabilities were then compared to calculate a false positive probability (FPP; the total probability of the transit originating from something other than a planet around the target star) and a nearby false positive probability (NFPP; the total probability of the transit originating from a nearby resolved star). Given our follow-up photometry rules out nearby stars as a potential source of the transit signal, we eliminate all stars except the target in the TRICERATOPS analysis. As an additional constraint, we use the contrast curve from our follow-up speckle imaging as a direct input in TRICERATOPS. For the sake of reliability, we performed the calculation 20 times for the planet candidate and found FPP=0.0020. The low FPPs calculated using VESPA and TRICERATOPS are small enough to statistically validate TOI-1696.01 as a planet.

---

[21] https://github.com/timothydmorton/VESPA

[22] https://github.com/stevengiacalone/triceratops
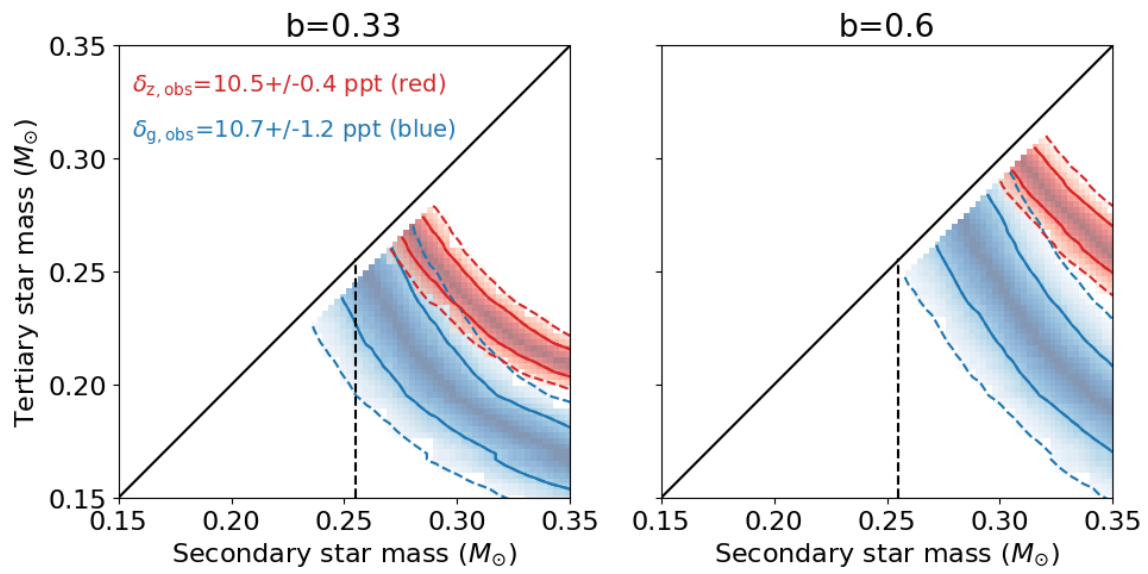
Figure C.2. HEB mass configurations which produce eclipse depths in g-band (blue) and z-band (red) consistent with the observed depths (indicated in the upper left corner of the first panel). The left panel corresponds to the lower limit of the impact parameter and the right for the median value. The colored solid line and dashed lines correspond to confidence regions that are consistent with the observed depths within 1- and 2-σ, respectively. The vertical black line corresponds to the mass of the central star (i.e. TOI-1696). The fact that the red and blue regions do not overlap within 1-σ taking into account impact parameter rules out the HEB false positive scenario.

REFERENCES

Anderson, O. L., Dubrovinsky, L., Saxena, S. K., & LeBihan, T. 2001, Geophys. Res. Lett., 28, 399, doi: 10.1029/2000GL008544

Astropy Collaboration, Robitaille, T. P., Tollerud, E. J., et al. 2013, A&A, 558, A33, doi: 10.1051/0004-6361/201322068

Astropy Collaboration, Price-Whelan, A. M., Sipőcz, B. M., et al. 2018, AJ, 156, 123, doi: 10.3847/1538-3881/aabc4f

Bellm, E. C., Kulkarni, S. R., Graham, M. J., et al. 2019, PASP, 131, 018002, doi: 10.1088/1538-3873/aaecbe

Belokurov, V., Penoyre, Z., Oh, S., et al. 2020, MNRAS, 496, 1922, doi: 10.1093/mnras/staa1522

Borucki, W. J., Koch, D., Basri, G., et al. 2010, Science, 327, 977, doi: 10.1126/science.1185402

Bouma, L. G., Hartman, J. D., Brahm, R., et al. 2020, AJ, 160, 239, doi: 10.3847/1538-3881/abb9ab

Brande, J., Crossfield, I. J. M., Kreidberg, L., et al. 2022, arXiv e-prints, arXiv:2201.04197. https://arxiv.org/abs/2201.04197

Brown, T. M., Baliber, N., Bianco, F. B., et al. 2013, PASP, 125, 1031, doi: 10.1086/673168

Burrows, A., Heng, K., & Nampaisarn, T. 2011, ApJ, 736, 47, doi: 10.1088/0004-637X/736/1/47

Castro González, A., Díez Alonso, E., Menéndez Blanco, J., et al. 2020, MNRAS, 499, 5416, doi: 10.1093/mnras/staa2353

Charbonneau, D., Berta, Z. K., Irwin, J., et al. 2009, Nature, 462, 891, doi: 10.1038/nature08679

Claret, A. 2017, A&A, 600, A30, doi: 10.1051/0004-6361/201629705

Claret, A., Hauschildt, P. H., & Witte, S. 2012, VizieR Online Data Catalog, 354

Cointepas, M., Almenara, J. M., Bonfils, X., et al. 2021, A&A, 650, A145, doi: 10.1051/0004-6361/202140328

Collins, K. A., Kielkopf, J. F., Stassun, K. G., & Hessman, F. V. 2017, AJ, 153, 77, doi: 10.3847/1538-3881/153/2/77

Cushing, M. C., Vacca, W. D., & Rayner, J. T. 2004, PASP, 116, 362, doi: 10.1086/382907

Cutri, R. M., Wright, E. L., Conrow, T., et al. 2021, VizieR Online Data Catalog, II/328

de Leon, J. P., Livingston, J., Endl, M., et al. 2021, arXiv e-prints, arXiv:2108.05621. https://arxiv.org/abs/2108.05621

Dressing, C. D., Hardegree-Ullman, K., Schlieder, J. E., et al. 2019, AJ, 158, 87, doi: 10.3847/1538-3881/ab2895

Erkaev, N. V., Kulikov, Y. N., Lammer, H., et al. 2007, A&A, 472, 329, doi: 10.1051/0004-6361:20066929

Foreman-Mackey, D. 2018, Research Notes of the American Astronomical Society, 2, 31, doi: 10.3847/2515-5172/aaaf6c

Foreman-Mackey, D., Agol, E., Ambikasaran, S., & Angus, R. 2017, AJ, 154, 220, doi: 10.3847/1538-3881/aa9332

Foreman-Mackey, D., Barentsen, G., & Barclay, T. 2019, dfm/exoplanet: exoplanet v0.1.5, doi: 10.5281/zenodo.2587222

Fukui, A., Narita, N., Tristram, P. J., et al. 2011, PASJ, 63, 287, doi: 10.1093/pasj/63.1.287

Gagné, J., Mamajek, E. E., Malo, L., et al. 2018, ApJ, 856, 23, doi: 10.3847/1538-4357/aaae09

Giacalone, S., & Dressing, C. D. 2020, arXiv e-prints, arXiv:2002.00691. https://arxiv.org/abs/2002.00691

Giacalone, S., Dressing, C. D., Jensen, E. L. N., et al. 2021, AJ, 161, 24, doi: 10.3847/1538-3881/abc6af

Girardi, L., Groenewegen, M. A. T., Hatziminaoglou, E., & da Costa, L. 2005, A&A, 436, 895, doi: 10.1051/0004-6361:20042352

Guerrero, N. M., Seager, S., Huang, C. X., et al. 2021, ApJS, 254, 39, doi: 10.3847/1538-4365/abefe1

Hayward, T. L., Brandl, B., Pirger, B., et al. 2001, PASP, 113, 105, doi: 10.1086/317969

Hippke, M., & Heller, R. 2019, A&A, 623, A39, doi: 10.1051/0004-6361/201834672

Hirano, T., Kuzuhara, M., Kotani, T., et al. 2020, PASJ, 72, 93, doi: 10.1093/pasj/psaa085

Hirano, T., Livingston, J. H., Fukui, A., et al. 2021, AJ, 162, 161, doi: 10.3847/1538-3881/ac0fdc

Hoffman, M. D., & Gelman, A. 2014, Journal of Machine Learning Research, 15, 1593

Howell, S. B., Everett, M. E., Sherry, W., Horch, E., & Ciardi, D. R. 2011, AJ, 142, 19, doi: 10.1088/0004-6256/142/1/19

Ionov, D. E., & Shematovich, V. I. 2015, Solar System Research, 49, 339, doi: 10.1134/S0038094615050056

Ishikawa, H. T., Aoki, W., Kotani, T., et al. 2020, PASJ, 72, 102, doi: 10.1093/pasj/psaa101

Ishikawa, H. T., Aoki, W., Hirano, T., et al. 2022, AJ, 163, 72, doi: 10.3847/1538-3881/ac3ee0

Jackson, A. P., Davis, T. A., & Wheatley, P. J. 2012, MNRAS, 422, 2024, doi: 10.1111/j.1365-2966.2012.20657.x

Jenkins, J. M. 2002, ApJ, 575, 493, doi: 10.1086/341136

Jenkins, J. M., & et al. 2020, Kepler Science Document KSCI-19081-003, Kepler Science Document KSCI-19081-003

Jenkins, J. M., Chandrasekaran, H., McCauliff, S. D., et al. 2010, in Society of Photo-Optical Instrumentation Engineers (SPIE) Conference Series, Vol. 7740, Software and Cyberinfrastructure for Astronomy, ed. N. M. Radziwill & A. Bridger, 77400D, doi: 10.1117/12.856764

Jenkins, J. S., Díaz, M. R., Kurtovic, N. T., et al. 2020, Nature Astronomy, 4, 1148, doi: 10.1038/s41550-020-1142-z

Kanodia, S., Wolfgang, A., Stefansson, G. K., Ning, B., & Mahadevan, S. 2019, ApJ, 882, 38, doi: 10.3847/1538-4357/ab334c

Karki, B. B., Wentzcovitch, R. M., de Gironcoli, S., & Baroni, S. 2000, PhRvB, 62, 14750, doi: 10.1103/PhysRevB.62.14750

Kempton, E. M. R., Bean, J. L., Louie, D. R., et al. 2018, PASP, 130, 114401, doi: 10.1088/1538-3873/aadf6f

Kipping, D. M. 2013, MNRAS, 435, 2152, doi: 10.1093/mnras/stt1435

Kochanek, C. S., Shappee, B. J., Stanek, K. Z., et al. 2017, PASP, 129, 104502, doi: 10.1088/1538-3873/aa80d9

Kotani, T., Tamura, M., Nishikawa, J., et al. 2018, in Society of Photo-Optical Instrumentation Engineers (SPIE) Conference Series, Vol. 10702, Ground-based and Airborne Instrumentation for Astronomy VII, ed. C. J. Evans, L. Simard, & H. Takami, 1070211, doi: 10.1117/12.2311836

Kuzuhara, M., Hirano, T., Kotani, T., et al. 2018, in Society of Photo-Optical Instrumentation Engineers (SPIE) Conference Series, Vol. 10702, Ground-based and Airborne Instrumentation for Astronomy VII, ed. C. J. Evans, L. Simard, & H. Takami, 1070260, doi: 10.1117/12.2311832

Li, J., Tenenbaum, P., Twicken, J. D., et al. 2019, PASP, 131, 024506, doi: 10.1088/1538-3873/aaf44d

Livingston, J. H., Crossfield, I. J. M., Petigura, E. A., et al. 2018, AJ, 156, 277, doi: 10.3847/1538-3881/aae778

Lopez, E. D. 2017, MNRAS, 472, 245, doi: 10.1093/mnras/stx1558

Luger, R., Agol, E., Foreman-Mackey, D., et al. 2019, AJ, 157, 64, doi: 10.3847/1538-3881/aae8e5

Mann, A. W., Brewer, J. M., Gaidos, E., Lépine, S., & Hilton, E. J. 2013, AJ, 145, 52, doi: 10.1088/0004-6256/145/2/52

Mann, A. W., Feiden, G. A., Gaidos, E., Boyajian, T., & von Braun, K. 2015, ApJ, 804, 64, doi: 10.1088/0004-637X/804/1/64

Mann, A. W., Gaidos, E., Mace, G. N., et al. 2016, ApJ, 818, 46, doi: 10.3847/0004-637X/818/1/46

Mann, A. W., Dupuy, T., Kraus, A. L., et al. 2019, ApJ, 871, 63, doi: 10.3847/1538-4357/aaf3bc

Masci, F. J., Laher, R. R., Rusholme, B., et al. 2019, PASP, 131, 018003, doi: 10.1088/1538-3873/aae8ac

Mazeh, T., Holczer, T., & Faigler, S. 2016, A&A, 589, A75, doi: 10.1051/0004-6361/201528065

McCully, C., Volgenau, N. H., Harbeck, D.-R., et al. 2018, in Society of Photo-Optical Instrumentation Engineers (SPIE) Conference Series, Vol. 10707, Software and Cyberinfrastructure for Astronomy V, ed. J. C. Guzman & J. Ibsen, 107070K, doi: 10.1117/12.2314340

Morton, T. D. 2015, VESPA: False positive probabilities calculator. http://ascl.net/1503.011

Morton, T. D., Bryson, S. T., Coughlin, J. L., et al. 2016, ApJ, 822, 86, doi: 10.3847/0004-637X/822/2/86

Muiños, J. L., & Evans, D. W. 2014, Astronomische Nachrichten, 335, 367, doi: 10.1002/asna.201312045

Murgas, F., Astudillo-Defru, N., Bonfils, X., et al. 2021, A&A, 653, A60, doi: 10.1051/0004-6361/202140718

Narita, N., Fukui, A., Kusakabe, N., et al. 2015, Journal of Astronomical Telescopes, Instruments, and Systems, 1, 045001, doi: 10.1117/1.JATIS.1.4.045001

Narita, N., Fukui, A., Yamamuro, T., et al. 2020, in Society of Photo-Optical Instrumentation Engineers (SPIE) Conference Series, Vol. 11447, Society of Photo-Optical Instrumentation Engineers (SPIE) Conference Series, 114475K, doi: 10.1117/12.2559947

Newton, E. R., Charbonneau, D., Irwin, J., et al. 2014, AJ, 147, 20, doi: 10.1088/0004-6256/147/1/20

—. 2022, tellrv: Radial velocities for low-resolution NIR spectra. http://ascl.net/2201.007

Nocedal, J., & Wright, S. J. 2006, Numerical Optimization, 2nd edn. (New York, NY, USA: Springer)

Owen, J. E., & Wu, Y. 2017, ApJ, 847, 29, doi: 10.3847/1538-4357/aa890a

Parviainen, H., Palle, E., Zapatero-Osorio, M. R., et al. 2020, A&A, 633, A28, doi: 10.1051/0004-6361/201935958

—. 2021, A&A, 645, A16, doi: 10.1051/0004-6361/202038934

Pecaut, M. J., & Mamajek, E. E. 2013, ApJS, 208, 9, doi: 10.1088/0067-0049/208/1/9

Rasmussen, C. E., & Williams, C. K. I. 2005, Gaussian Processes for Machine Learning (Adaptive Computation and Machine Learning) (The MIT Press)

Rayner, J. T., Toomey, D. W., Onaka, P. M., et al. 2003, PASP, 115, 362, doi: 10.1086/367745

Reid, I. N., Brewer, C., Brucato, R. J., et al. 1991, PASP, 103, 661, doi: 10.1086/132866

Ricker, G. R., Winn, J. N., Vanderspek, R., et al. 2015, Journal of Astronomical Telescopes, Instruments, and Systems, 1, 014003, doi: 10.1117/1.JATIS.1.1.014003

Rogers, L. A. 2015, ApJ, 801, 41, doi: 10.1088/0004-637X/801/1/41

Salpeter, E. E., & Zapolsky, H. S. 1967, Physical Review, 158, 876, doi: 10.1103/PhysRev.158.876

Salvatier, J., Wiecki, T. V., & Fonnesbeck, C. 2016, PeerJ Computer Science, 2, e55

Saumon, D., Chabrier, G., & van Horn, H. M. 1995, ApJS, 99, 713, doi: 10.1086/192204

Scott, N. J. 2019, in AAS/Division for Extreme Solar Systems Abstracts, Vol. 51, AAS/Division for Extreme Solar Systems Abstracts, 330.15

Seager, S., Kuchner, M., Hier-Majumder, C. A., & Militzer, B. 2007, ApJ, 669, 1279, doi: 10.1086/521346

Shematovich, V. I., Ionov, D. E., & Lammer, H. 2014, A&A, 571, A94, doi: 10.1051/0004-6361/201423573

Skrutskie, M. F., Cutri, R. M., Stiening, R., et al. 2006, AJ, 131, 1163, doi: 10.1086/498708

Smith, J. C., Stumpe, M. C., Van Cleve, J. E., et al. 2012, PASP, 124, 1000, doi: 10.1086/667697

Stassun, K. G., Collins, K. A., & Gaudi, B. S. 2017, AJ, 153, 136, doi: 10.3847/1538-3881/aa5df3

Stassun, K. G., & Torres, G. 2016, AJ, 152, 180, doi: 10.3847/0004-6256/152/6/180

—. 2021, ApJL, 907, L33, doi: 10.3847/2041-8213/abdaad

Stassun, K. G., Oelkers, R. J., Pepper, J., et al. 2018, AJ, 156, 102, doi: 10.3847/1538-3881/aad050

Stumpe, M. C., Smith, J. C., Catanzarite, J. H., et al. 2014, PASP, 126, 100, doi: 10.1086/674989

Stumpe, M. C., Smith, J. C., Van Cleve, J. E., et al. 2012, PASP, 124, 985, doi: 10.1086/667698

Szabó, G. M., & Kiss, L. L. 2011, ApJL, 727, L44, doi: 10.1088/2041-8205/727/2/L44

Tamura, M., Suto, H., Nishikawa, J., et al. 2012, in Society of Photo-Optical Instrumentation Engineers (SPIE) Conference Series, Vol. 8446, Ground-based and Airborne Instrumentation for Astronomy IV, ed. I. S. McLean, S. K. Ramsay, & H. Takami, 84461T, doi: 10.1117/12.925885

Tody, D. 1993, in Astronomical Society of the Pacific Conference Series, Vol. 52, Astronomical Data Analysis Software and Systems II, ed. R. J. Hanisch, R. J. V. Brissenden, & J. Barnes, 173

Toledo-Padrón, B., González Hernández, J. I., Rodríguez-López, C., et al. 2019, MNRAS, 488, 5145, doi: 10.1093/mnras/stz1975

Twicken, J. D., Catanzarite, J. H., Clarke, B. D.,
et al. 2018, PASP, 130, 064502,
doi: 10.1088/1538-3873/aab694

Vacca, W. D., Cushing, M. C., & Rayner, J. T.
2003, PASP, 115, 389, doi: 10.1086/346193

Watson, A. J., Donahue, T. M., & Walker,
J. C. G. 1981, Icarus, 48, 150,
doi: 10.1016/0019-1035(81)90101-9

Weiss, L. M., & Marcy, G. W. 2014, ApJL, 783,
L6, doi: 10.1088/2041-8205/783/1/L6

Wells, R. D., Rackham, B. V., Schanche, N., et al.
2021, A&A, 653, A97,
doi: 10.1051/0004-6361/202141277

West, R. G., Gillen, E., Bayliss, D., et al. 2019,
MNRAS, 486, 5094,
doi: 10.1093/mnras/stz1084

Zeng, L., & Sasselov, D. 2013, PASP, 125, 227,
doi: 10.1086/669163